Journal of Catalysis 425 (2023) 406–421

Contents lists available at ScienceDirect

Journal of Catalysis

journal homepage: www.elsevier.com/locate/jcat

Molecular-level understanding of interfacial carbonates in stabilizing CuO-ZnO(Al_2O_3) catalysts

Aleksandar Živković [a,1,*], Vanessa Solsona-Delgado [b,1], Bart van der Linden [b,c], Nora H. de Leeuw [a,d], Ignacio Melián-Cabrera [b,e,*]

[a] Department of Earth Sciences, Utrecht University, Princetonlaan 8a, 3584CB Utrecht, the Netherlands
[b] DelftChemTech, Delft University of Technology, Julianalaan 136, 2628 BL Delft, the Netherlands
[c] Catalysis Engineering, Chemical Engineering Department, Faculty of Applied Sciences, Delft University of Technology, Van der Maasweg 9, 2629 HZ Delft, the Netherlands
[d] School of Chemistry, University of Leeds, Wodehouse Lane, Leeds LS2 9JT, United Kingdom
[e] Applied Photochemistry and Materials for Energy Group, University of La Laguna, Avda. Astrofísico Francisco Sánchez, s/n, PO BOX 456, 38200 San Cristóbal de La Laguna, S/C de Tenerife, Spain

ARTICLE INFO

Article history:
Received 11 April 2023
Revised 24 May 2023
Accepted 25 June 2023
Available online 26 June 2023

Keywords:
Methanol synthesis catalysts
CuO-ZnO catalysts
High-temperature-carbonate descriptor
Thermal sintering
Structural stability
First-principles calculations

ABSTRACT

A descriptor of active CuO-ZnO(Al_2O_3) methanol-synthesis and water–gas-shift catalysts is the presence of high-temperature carbonates (HT-CO_3) in the oxidic catalyst precursor. Previous reports have shown that such HT-CO_3 lead to an appropriate interaction between the oxides; as a result, a high Cu surface area (or Cu-Zn or Cu/ZnO interphase areas) can be achieved. Yet, their nature is not well understood. In this study, the nature of these carbonates was investigated by experimental and theoretical methods in the oxidic precatalyst. A calcined Cu-Zn-Al hydrotalcite model compound revealed to have well-dispersed ZnO and CuO phases, together with highly stable HT-CO_3. It was hypothesized that these HT-CO_3 groups may be placed at critical locations at nano-scale as a glue, thus avoiding the growth of the oxide crystallites during calcination. This is an excellent pre-condition to achieve a high Cu surface area (or Cu-Zn or Cu/ZnO interphase areas) upon reduction, and therefore a high activity. To prove that, first-principles calculations were carried out based on the density functional theory (DFT); alumina was not considered in the model as the experimental data showed it to be amorphous but it may still have an effect. Comprehensive calculations provided evidence that such carbonate groups favourably bind the CuO and ZnO together at the interface, rather than being isolated on the individual oxide surfaces. The results strongly suggest that the HT-CO_3 groups are part of the structure, in the calcined precatalyst, where they would prevent thermal sintering through a bonding mechanism between CuO and ZnO particles, which is a novel interpretation of this important catalyst descriptor.

1. Introduction

Copper not only plays a significant role in synthetic catalysis, but is also essential for life, with a number of proteins and enzymes containing Cu [1]. In organic synthesis, copper compounds have been used as catalysts for reactions such as amination and ether formation from aryl halides and related compounds, aziridination of olefins, "click-chemistry", hydrosilylation reactions, and additions to carbonyl and α,β-unsaturated carbonyl compounds [2]. In heterogeneous catalysis, Cu in combination with ZnO has been crucial in industrial processes such as methanol synthesis [3–12], the low-temperature water gas shift reaction [11,13], H_2 production [14], and hydrogenation of various types of organic compounds [15,16]. These catalysts have become of interest again, in view of contemporary efforts to convert CO_2 into chemicals/fuels, in combination with H_2 from renewable sources [17,18]. Alumina is usually added to CuO-ZnO to enhance the catalyst stability by preventing the sintering of the Cu crystallites[19], although it has been shown that this affects the ZnO as well [8] (here, a clear promoting effect of Al on the methanol yield was proven).

The synthesis of these catalysts is normally carried out by co-precipitation, which generates well-defined mixed metal com-

* Corresponding authors at: Department of Earth Sciences, Utrecht University, Princetonlaan 8a, 3584CB Utrecht, The Netherlands (A. Živković); Applied Photochemistry and Materials for Energy Group, University of La Laguna, Avda. Astrofísico Francisco Sánchez, s/n, PO BOX 456, 38200 San Cristóbal de La Laguna, S/C de Tenerife, Spain (I. Melián-Cabrera).
E-mail addresses: a.zivkovic@uu.nl (A. Živković), ignacio.melian.cabrera@ull.edu.es (I. Melián-Cabrera).
[1] Authors contributed equally.

https://doi.org/10.1016/j.jcat.2023.06.032
0021-9517/

pounds, denoted as hydroxycarbonates and hydrotalcites. Calcination of these compounds allows the formation of inter-dispersed CuO-ZnO or CuO-ZnO(Al_2O_3) phases. The reductive activation of the calcined precursors produces catalysts with a high metal copper surface area, Cu-Zn or Cu/ZnO interphase areas, which are descriptors of the methanol synthesis reaction with CO or CO_2, or both. The role of ZnO has been extensively investigated, as it acts as a spacer between the Cu crystallites, to maximize the metallic surface area. It also participates in the active site model, as a Cu-Zn alloy [10,20,21], or provides interfacial synergy as Cu/ZnO [17,18] where the pre-reduced Zn is oxidized under reaction in the vicinity of Cu, as ZnO [17] or Zn-formate [18]. ZnO is also important for stability purposes since it acts as sulphur scavenger to protect the Cu crystallites; this happens at the top of the reactor bed if there is no guard bed or one that fails [22]. The main challenge for this system in the methanol synthesis from CO_2 is that this reaction produces H_2O, and H_2O leads to catalyst deactivation. At high conversion, a volcano-type behaviour can be observed for the dependence of methanol formation on the CO:CO_2 ratio in the feed gas demonstrating the inhibition by water [23,24]. In terms of stability, water can possibly be involved by damaging the synergistic Cu-ZnO interaction by inducing sintering of these catalyst domains [25–27]. Sintering leads to the segregation of Cu and ZnO, thereby suppressing the strong metal-support interaction effect. This is a key area for further improvement, although it is outside the scope of this paper.

Although the CuO-ZnO(Al_2O_3) system has been used industrially for many decades, more recent and significant further academic progress has revealed that the topic still faces important challenges. For instance, attractive synthetic approaches have been developed with various practical goals, e.g. continuous synthesis using a micro-mixer [28], use of supercritical fluids [9,11,29], lowering the amount of wastewater [30], lessening the detrimental effect of Na with alternative hydroxycarbonates [29], a new class of Cu/ZnO derived catalysts from novel synthetic routes [9,11,29,31], improved stability by controlling Cu sintering using model systems [32], and understanding the reductive activation [33,34]. As such, understanding the catalyst synthesis and its structure at the various steps (i.e., calcination, activation, and reaction) is still a highly active research area aimed at improving this catalysed processes. It is well-known that the final Cu dispersion or Cu-based active sites are the consequence of the full experimental trajectory from the hydroxycarbonate/hydrotalcite structure, calcination, and reduction conditions. This study focuses on the intermediate calcined material, also denoted as precatalyst.

One important descriptor that predicts how good a CuO-ZnO (Al_2O_3) catalyst is, is the presence of 'high-temperature carbonates' (HT-CO_3), which can be detected by thermo-gravimetric analysis of the starting hydroxycarbonate [35,36]. Millar et al. [36] originally proposed that carbonate-modified oxides may lead to extra stabilization of both small copper oxide and zinc oxide particles. HT-CO_3 have been confirmed by independent groups to be beneficial in catalysed reactions; methanol synthesis and water gas shift reactions [5,11,28,29,37,38]. The role of these species has also been discussed in characterization studies [33,39,40]. Such carbonate groups come from particular hydroxycarbonate/hydrotalcite compounds whose carbonate decomposition occurs at high temperatures (ca. 450–600 °C) and they remain in the structure after the typically-applied calcination at 300–400 °C. The latter temperature window is used to avoid the sintering of the CuO-ZnO(Al_2O_3) phases, and therefore circumvents the occurrence of a low Cu surface area, or less active sites, in the reduced state before reaction.

These residual carbonates are believed to have a positive stabilization effect during calcination, which avoid or reduce sintering of the oxidic phases but also during the CuO reduction. Having sintering in the oxide or metal formation will result in a low copper surface area (or Cu-Zn or Cu-ZnO interphase areas) and low(er) activity or stability; note that generally the specific Cu surface area alone does not adequately account for the catalytic activity, since methanol synthesis over Cu-based catalysts has been identified to be a structure-sensitive reaction as exemplified above with various models[10,17,18,20,21]. By studying the microstructural properties of Cu-Zn hydroxycarbonates, Bems et al. [39] proposed that these HT-CO_3 may serve as a growth inhibitor for the oxide crystallites. Additional studies have shown that these HT-CO_3 are not exclusive to synthetic materials, as they are also found in natural Cu-Zn minerals [40]. It has also been proposed that such carbonates (detected in binary Cu-Zn hydroxycarbonates) are trapped at the CuO-ZnO interfaces, where they provide stable grain boundaries [40]. These findings also imply that these groups act as growth inhibitors of the oxides during sintering, as suggested by Bems et al. [39]. An interesting observation was reported by Kühl et al. [37], who attributed the stabilizing effect of such HT-CO_3 to the material's texture, since the surface area between the hydrotalcite (89 m^2/g) and the HT-CO_3-containing calcined material hardly changed (81 m^2/g). The surface area was only lowered upon removal of the carbonates at 700 °C (38 m^2/g). In terms of catalysis, such HT-CO_3 groups play a role in the intrinsic activity, as clearly shown by Schur et al. [28], but also in the stability, as clearly proven by Schumann et al. [38]. The latter reported that the HT-CO_3-free catalyst deactivated quite fast compared to the HT-CO_3-containing catalysts. But they also found that the type of carbonate was crucial; catalysts containing free non-coordinating carbonates (deduced from IR analysis) deactivate faster than catalysts containing coordinating carbonates (in the calcined catalysts). As far as the reduced catalysts are concerned, the HT-CO_3 are able to slow down the reduction of CuO; this took place at higher temperatures when the HT-CO_3 species were present, hence providing some sort of stabilisation[41]. High-resolution TEM on reduced Cu/ZnO:Al catalysts evidenced phase separation tendencies between Cu and ZnO when HT-CO_3 was absent [33]. Despite the clear evidence of the importance of these species in catalyst activity and/or stability, there is hardly any information in the literature on the molecular structure, particularly how they bind the oxide domains to prevent or reduce sintering.

In this work, we have investigated the nature of these HT-CO_3 using a well-defined structure, a Cu-Zn-Al hydrotalcite, with supporting first-principles calculations. Experimentally, the aim was to study in more detail the nature of the HT-CO_3 by means of XRD, thermal methods, IR spectroscopy and a thermo-kinetic study. With that experimental information, we found that the structure after calcination is an oxy-carbonate, where the carbonate groups are stable and may take part in the structure due to the high decomposition temperature, high activation energy during its decomposition and IR spectrum showing strongly coordinating and asymmetric carbonates. Calculations based on the density functional theory (DFT) on model systems support the hypothesis that such HT-CO_3 act as a growth inhibitor by holding the CuO and ZnO domains together. The role of the Al_2O_3 was not considered in the DFT model as the experimental data showed it to be amorphous, but it could have an additional impact during the calcination (and by extension in the reduction, not studied here). This study provides a novel molecular interpretation of these crucial species in the calcined precatalyst.

2. Methods

2.1. Experimental methods

2.1.1. Chemicals

The following analytical-grade chemicals were employed for the synthesis of the hydrotalcite: $Cu(NO_3)_2{\cdot}3H_2O$, 99.5% Merck;

$Zn(NO_3)_2{\cdot}6H_2O$, 99.0% J.T. Baker; $Al(NO_3)_3{\cdot}9H_2O$, 98.5% Merck; Na_2CO_3 (99.5%) and NaOH (99.0%) were acquired from J.T. Baker.

2.1.2. Synthesis of the hydrotalcite

The Cu-Zn-Al hydrotalcite-like compound, $(Cu,Zn)_6Al_2(OH)_{16}CO_3{\cdot}4H_2O$, was prepared at pH = 9 using a mixture of NaOH/Na_2CO_3. A solution containing the metal nitrates (Cu^{2+} + Zn^{2+} + Al^{3+} = 1.0 M) was continuously added into a Na_2CO_3 aqueous solution (Al^{3+}/CO_3^{2-} = 2), initially placed in the reaction vessel. The mixture was kept at constant pH (ca. 9.0) by drop-wise addition of a NaOH aqueous solution (2.0 M), using a pH Stato® set-up. The temperature was kept at 70 °C and the suspension was magnetically stirred at 750 rpm. The final suspension was aged for 24 h under a milder stirring (300 rpm) at the synthesis temperature. The precipitate was filtered and repeatedly washed with distilled water to remove residual sodium. The nominal molar composition of the hydrotalcite was Cu:Zn:Al = 25:50:25.

2.1.3. Thermal activation

The precursor was calcined in a shallow-bed configuration under static air at 350 °C for 4 h at a heating rate of 2 °C/min.

2.1.4. Elemental analysis

The chemical composition of the elements copper, zinc, aluminum and sodium of the calcined material was determined by ICP-OES technique using a Perkin Elmer Optima 4300DV spectrometer. The solid sample was previously digested in concentrated HNO_3 and diluted afterwards in water to operate within the calibration curve. The experimental error was less than 3% relative.

2.1.5. Thermal analysis

Thermogravimetric analysis (TGA) was carried out in a TGA/SDTA851e Mettler-Toledo analyzer. The sample holder (70 μL α-Al_2O_3) was loaded with 15–35 mg of material, and the weight loss was monitored in a flow of synthetic air of 100 ml/min (STP). The temperature was increased from 30 to 800 °C at various heating rates. The sample pattern was corrected with a blank curve, using an empty sample holder. The activation energies were determined by two methods. The Ozawa-Flynn-Wall model [42] is given by equation (1):

$$\frac{d(\log \beta i)}{d(1/T_X)} \approx -0.4567\left(\frac{E_{ACT}}{R}\right) \quad (1)$$

where β_i is the heating rate (K/min) and T_X is the temperature in Kelvin at *iso*-conversion. Therefore, the plot of log(β_i) versus $1/T_X$ gives the value of the activation energy from the slope. This calculation was done at various conversions and an average value was reported for each step. The Kissinger model [42] is given by equation (2):

$$\frac{d\ln\left(\frac{\beta i}{T_M^2}\right)}{d(1/T_M)} = -\left(\frac{E_{ACT}}{R}\right) \quad (2)$$

where β_i is the heating rate (K/min) and T_M is the temperature in Kelvin of the maxima for each decomposition step in the DTGA pattern, for each heating rate. Therefore, the Kissinger method is applied to individual and well-resolved peaks in the DTGA. The activation energy is derived from the slope of the representation of $\ln\left(\frac{\beta i}{T_M^2}\right)$ versus $1/T_M$.

2.1.6. Analysis of the gaseous products during thermal decomposition

Analysis of the evolved gases during the thermal decomposition was performed by mass spectrometry (EGA-*ms*) in a home-made fixed-bed reactor (4 mm ID) set-up using a ca. 21 vol% O_2/helium mixture as carrier gas (ca. 45 ml/min STP), equipped with a Pfeiffer quadrupole mass spectrometer. The temperature was increased from 30 to 800 °C at 10 °C/min while the composition of gases was analyzed. The samples were diluted with SiC to improve heat transfer in the bed. The fragments m/z = 18 (H_2O) and m/z = 44 (CO_2) were analysed.

2.1.7. IR analysis

FTIR spectra (DRIFT, diffuse reflectance infrared Fourier transform spectroscopy) of the hydrotalcite and calcined counterpart were collected on a Nicolet Magna 860 spectrometer, equipped with a DTGS detector and a Praying Mantis™ Harrick DRIFT cell [43]. The spectra were acquired by co-addition of 256 scans with a resolution of 4 cm^{-1}. The material (ca. 30 mg) was loaded in the sample holder and, after closing the dome, dry air was passed over the sample for a prolonged time to remove moisture present in the cell. The spectrum of the hydrotalcite was taken at 30 °C (after drying it at 100 °C for 2 h to stabilize the water level; if this step is not done, the stabilization requires a much longer period. The calcined sample's spectrum was taken at 30 °C after being treated in air at 350 °C for 3 h using a heating rate of 10 °C/min. A DRIFT spectrum of an in situ dried KBr (Aldrich, FTIR grade) was used as background.

2.1.8. XRD diffraction

XRD patterns of the starting hydrotalcite and calcined counterpart were measured in a Bruker-Nonius D-5005 diffractometer equipped with a graphite monochromator. A CoKα X-ray source was used, and data were collected in the range of 7 to 85 (2θ, degree) with a step size of 0.02° (2θ) and a counting time of 2 s (step mode). The angle coordinate was corrected mathematically into the CuKα scale. The JCPDS database was used for the identification of the crystalline phases.

2.1.9. temperature-programmed H_2 reduction

The temperature-programmed H_2 reduction profile was carried out according to the procedure and equipment described earlier by Solsona et al. [44].

2.2. Computational methods

Density functional theory (DFT) calculations were performed using the all-electron (AE) code CRYSTAL17 [45–48]. The global B3LYP hybrid functional [49,50] was employed together with basis sets based on Gaussian-type orbitals (GTOs), for which the following were employed: Zn constructed and optimized by Jaffe et al. [51,52], Cu from Doll et al. [53], O by Valenzano et al. [54], Na from Dovesi et al. [55] and for C the 6-21G* from Dovesi et al. [56] In structural optimizations, both the atomic positions and the lattice constants were fully optimized within the constraints imposed by the space group symmetry. The reciprocal space was sampled using 9x9x7 and 5x13x5 Monkhorst-Pack type k-point grids for ZnO bulk and CuO bulk, respectively [57]. For the evaluation of the Coulomb and exchange integrals, the tolerance factor values of 8, 8, 8, 8, and 16 were used (TOLINTEG). Long range dispersion corrections were included using the semiempirical D3 approach of Grimme et al. with Becke-Johnson damping [58–60]. Band structure calculations were performed on optimized geometries along high-symmetry directions obtained using the SeeK-path interface [61,62]. Graphical drawings were produced using Ovito [63].

The surfaces (and interfaces) were modelled as a two-dimensional slab, and no three-dimensional periodicity was imposed. This means that there is no parameter for the vacuum thickness needed. To characterise the surface, the surface energy (γ) as a measure of the thermodynamic stability has been calculated through the following expression:

$$\gamma = \frac{E(n) - n \cdot E_{bulk}}{2 \cdot A} \quad (3)$$

where $E(n)$ is the energy of the slab containing n-layers, E_{bulk} the energy of the bulk, and A the area of the slab. The computed surface energies were obtained from standard DFT conditions, i.e., nominally zero Kelvin and ambient pressure without further thermodynamical consideration.

The binding energy (or adsorption energy) of the chosen adsorbates (E_b) was calculated from the fully relaxed geometries, through the following expression:

$$E_b = E_{slab+ads} - (E_{slab} + E_{ads}) \quad (4)$$

where $E_{slab+ads}$ is the total energy of the slab interacting with the absorbate, while E_{slab} and E_{ads} denote the total energies of the pristine surface and isolated adsorbate, respectively. Within this definition of the binding energy, a negative value represents a favourable exothermic process, while a positive energy corresponds to an endothermic process. When using atomic-centred localised basis sets, the binding energy is affected by the basis set superposition error (BSSE), which corresponds to an artificial increase (spurious extra-binding that mimics the dispersion energy) in the computed binding energy, because the basis set of the final system is larger than that of the component subsystems. One way to estimate the BSSE is using the counterpoise (CP) method, where one recalculates E_{slab} and E_{ads} by supplementing the basis set of each sub-system with all the basis functions of the other without their electrons and nuclei (referred to as "ghost functions"). The BSSE is a positive quantity and equals to:

$$BSSE = \left(E_{ads|system} - E^{G}_{ads|system}\right) + \left(E_{slab|system} + E^{G}_{slab|system}\right) \quad (5)$$

where $E^{G}_{ads|system}$ and $E^{G}_{slab|system}$ denote the energies of the adsorbate and surface calculated, respectively, in the presence of the "ghosted atoms" of the surface and of the adsorbate (i.e., including the extra basis set of the surface or the adsorbate). Taking into account the BSSE, the CP-corrected binding energy (E^{CP}_b) reads [64,65]:

$$E^{CP}_b = E_b + BSSE \quad (6)$$

Interface structures were produced using pymatgen [66–68], where the Zur and McGill lattice matching algorithm is employed [69]. The focus of this study is not on epitaxial interfaces, but rather the behaviour of the adsorbate between the layers. However, a suitable interface was chosen with ZnO acting as a film on top of a CuO substrate for the smallest possible lattice strain (5.8%) and area, resulting in a tractable simulation cell.

Transition state optimizations have been performed using the distinguished reaction coordinate (DRC) method, where one degree of freedom, called the distinguished coordinate, is chosen and kept fixed at a sequence of values that are representative of the reaction path, while other coordinates are relaxed for each of these values. Initially, a preliminary exploration of the potential energy hypersurface is performed by scanning along a selected valence internal coordinate using the valence redundant scheme [70]. The maximum-energy geometry along the path is then taken as the initial guess for the saddle-point search, as implemented in the DRC algorithm in CRYSTAL [71–73].

The specific adhesion energy (β), a measure of the gained energy once the interface boundary between two surfaces (S1 and S2) is formed, is given by:

$$\beta_{S1/S2} = \frac{E_{S1} + E_{S2} - E_{S1/S2}}{A} \quad (7)$$

where E_{S1} and E_{S2} are total energies of the respective slabs and $E_{S1/S2}$ is the final interface energy. Similarly, to the case of the computed binding energy, the adhesion energy is corrected for the BSSE by using the counterpoise method, yielding $\beta^{CP}_{S1/S2}$. Furthermore, the adhesion energy for the interface containing adsorbed carbonate species is an average quantity representing the energy gain once the two interfaces between three surfaces are formed, then expressed as:

$$\beta_{S1/CO_3/S2} = \frac{E_{S1} + E_{S2} + n \cdot E_{CO_3} - E_{S1/CO_3/S2}}{2A} \quad (8)$$

where E_{CO_3} is the total energy of the respective carbonate molecule, n the number of carbonate molecules present in the system, and $E_{S1/CO_3/S2}$ the total energy of the interface containing the carbonates.

Vibrational harmonic frequencies were calculated at the Γ-point and the corresponding infrared intensities for each normal mode obtained by computing the dipole moment variation along the normal mode evaluated through a Berry phase approach [47,48].

3. Results

3.1. Cu-Zn-Al hydrotalcite as model compound to obtain experimental insights

The general formula of hydrotalcite corresponds to a layered double hydroxide, given as $[M^{2+}_{1-x}M^{3+}_{x}(OH)_2]^{x+}[A^{n-}_{x/n}]^{x-}\cdot mH_2O$, where M^{2+} is a divalent cation, M^{3+} is a trivalent cation and A^{n-} is the anion, typically CO_3^{2-} if a carbonate is employed in their synthesis [74,75]. Hydrotalcites are usually studied as inorganic base catalysts [76,77]. On some occasions, the synthesis of a hydrotalcite is not aimed at producing a base catalyst itself but to achieve a high metal inter-dispersion that cannot be obtained by other methods. In that situation, a hydrotalcite provides a good metal oxide inter-dispersion after calcination, leading to minimal sintering, as found, for instance, in the case of the Cu-Zn-Al mixed oxide catalysts derived from hydrotalcites [37,78–81], that are employed for methanol synthesis and other applications. The benefit of a hydrotalcite for this study is the simpler IR spectrum to assess changes upon calcination. These are less obvious or undiscernible with Cu-Zn hydroxycarbonates. For instance, another model system could be aurichalcite. However, the IR interpretation is not helpful to show the HT-CO_3 coordination/insertion upon calcination. The hydrotalcite provides a more complete picture.

The Cu-Zn-Al hydrotalcite was synthesized by coprecipitation using metal nitrates and Na_2CO_3/NaOH as a precipitating agent at constant pH. The XRD pattern (Fig. 1A) shows the hydrotalcite structure (JCPDS 38–487) [79,82] as the sole crystalline phase with well-defined reflections. Note that an internal standard was used (a highly-crystalline silicon powder) for calibration purposes. Therefore, the reflections from Si are also visible. The elemental composition of the hydrotalcite (Table S1) is in agreement with the nominal molar composition with Cu:Zn = 0.49 and (Cu + Zn)/Al = 3.22. The latter is slightly higher than the nominal quantity, i.e., 3, which may be due to a deficiency in Al or an excess in (Cu + Zn), or both. Inspection of the individual molar composition shows a ratio of Cu:Zn:Al = 25.2:51.1:23.7 for nominal values of 25:50:25. Indeed, both situations occur; the Zn content is slightly higher and the Al is slightly smaller than the nominal values, which may be related to differences in the crystallization water content of the commercial hydrated nitrates employed in the synthesis.

The as-synthesized hydrotalcite was further characterized by FTIR where the main reflections have been highlighted (Fig. 2A). The band at 3500 cm^{-1} arises from the OH stretching mode from structural hydroxyl groups, water molecules in the interlayer zone, and loosely physisorbed free water on the external surface [75,83].

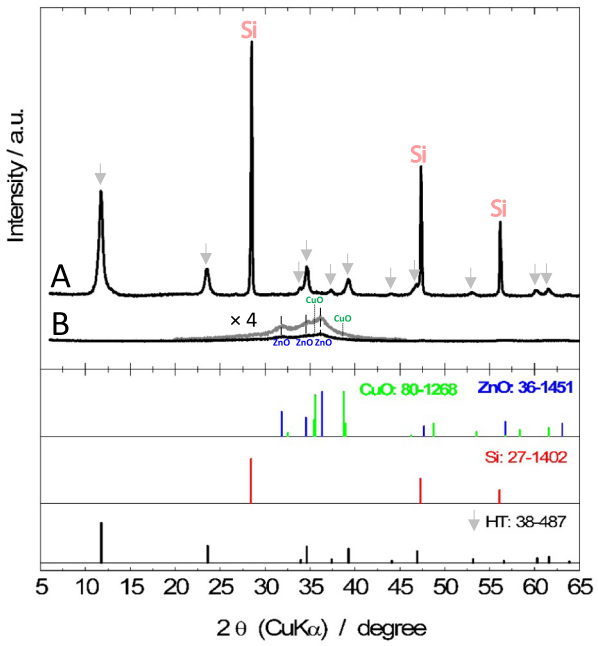

Fig. 1. XRD patterns of the as-synthesized Cu-Zn-Al hydrotalcite (**A**) and calcined hydrotalcite (**B**), including an amplification for the latter. Bottom) JCPDS files for reference materials (HT for hydrotalcite; silicon, CuO and ZnO). Si powder used as an internal standard. Figure S1 shows additional information about the CuO identification.

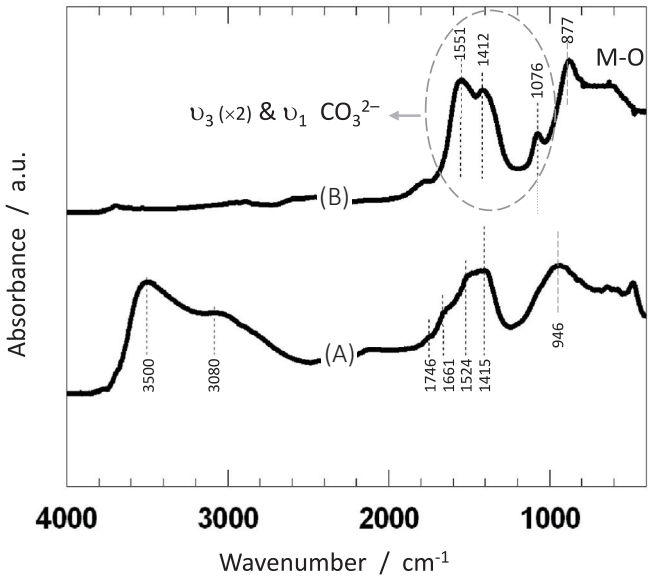

Fig. 2. *In situ* DRIFT spectra of the as-synthesized hydrotalcite, dried at 100 °C (**A**) and after synthetic air treatment at 350 °C (**B**).

The band at 3080 cm^{-1} is distinctive of hydrotalcite material, owing to the hydrogen bonding between the water molecules and the CO_3^{2-} groups present in the interlayer region [74]. The H–O–H bending can be seen at 1661 cm^{-1} (physisorbed water) [75] and 1746 cm^{-1} (interlayer water) [84]. Relevant carbonate vibrations are observed in the range 1400–1550 cm^{-1}, corresponding to the ν_3 mode (asymmetric stretching of the CO_3^{2-} anions) at 1415 cm^{-1}. The band at 1524 cm^{-1} comes from the loss of symmetry of the ν_3 mode due to removal of interlayer water and rearrangement of the carbonates either as mono- or bidentate coordination, between carbonates and structural hydroxyl groups [83–85]. However, since the band at 1746 cm^{-1} is present, the material has lost only part of the interlayer water, leading to a moderate splitting of the ν_3 mode. The partial interlayer dehydration originates from the mild drying that was applied prior to the IR recording, to minimize the water level in the mass spectrometer chamber. Melián-Cabrera et al. [83]. showed a more pronounced splitting, i.e., a more pronounced 1524 cm^{-1} band, at 150 °C due to the complete removal of the interlayer water.

The above experimental characterization shows that a well-defined Cu-Zn-Al hydrotalcite structure was formed.

Hydrotalcites are often activated, i.e., forming the corresponding oxide phases, by a thermal treatment in air where they undergo various decomposition processes. The thermal decomposition was studied by thermo-gravimetric analysis (TGA) combined with evolved gas analysis (EGA). The profiles are plotted in Fig. 3A, including the differential TGA (DTGA) to visualize better the decomposition steps. By comparing the DTGA profiles with the *m*/*z* fragments for H_2O and CO_2, there is very good agreement between both techniques, since the DTGA profiles mirror the *m*/*z* traces (i.e., the addition of both CO_2 and H_2O curves). The hydrotalcite decomposes in four steps (DTGA). The first step (denoted as α), with a maximum at ca. 150 °C, is principally due to the removal of the interlayer water (physisorbed free water on the external surface can also be present). This step was assigned in the literature considering that the interlayer space decreases, and such a reduction is associated with the loss of inter-lamellar water [86,87]. A second water-release process takes place between 200 and 350 °C (denoted as β) due to the removal of the structural OH groups [75]. It is evident that the only possible water release should come from the OH condensation, which has been confirmed by inspecting the water release of various hydroxides [88,89]. It was shown elsewhere that the dehydroxylation takes place in various stages [90], and we have therefore assigned a temperature range for such a β process. The CO_3^{2-} decomposition takes place in three stages. The first one starts at ca. 300 °C and is simultaneous with the dehydroxylation, whereas the other two take place above 550 °C (γ and δ, Fig. 3A). The presence of these high-temperature CO_3^{2-} (HT-CO_3) is a special feature compared to the conventional Mg-Al hydrotalcite, whose carbonates decompose at lower temperature (350–450 °C) [87–89]. These high-temperature carbonates have also been observed for Cu-Zn-Al hydrotalcites with a higher Cu content than ours, with decomposition peaks centred at ca. 616 °C [37], ca. 590 °C [91], between 550 and 625 °C [80] and ca. 510 °C [83]. Note that the decomposition temperature (peak position) depends on the experimental conditions. A comparison of the decomposition temperatures under equal conditions (i.e., using air and equal heating rate), including this work, reveals that the HT-CO_3 in hydrotalcites are in general more stable compared to binary (Cu-Zn) hydroxycarbonates [38,39,83], though in some cases they come close.

3.2. Structural features of the calcined Cu-Zn-Al hydrotalcite

The hydrotalcite was activated by calcination in air at 350 °C after which the structural features were assessed. The XRD pattern (Fig. 1B) shows broad reflections due to ZnO (JCPDS 36–1451), while CuO (JCPDS 80–1268) could be inferred in the shoulders of the broad ZnO reflections, where CuO reflections seem to be masked by the ZnO. Additional information about the CuO identification by XRD can be found in Figure S1 using reference materials. Note that Cu(II) can be present as CuO but also, in part, as oxycarbonate (as can Zn(II)). The Cu(II) concentration is lower than Zn(II), but the CuO concentration could be even lower due to the

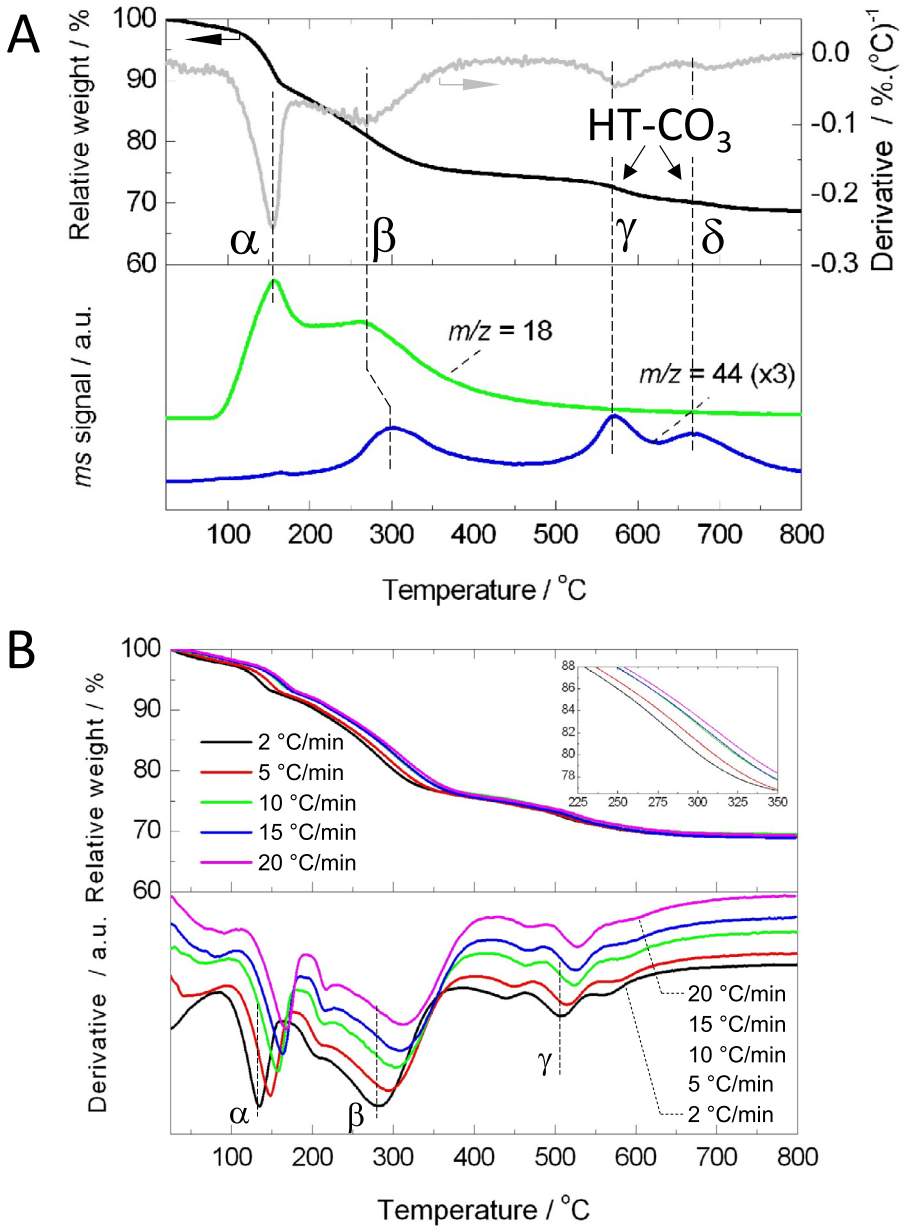

Fig. 3. A) Thermal decomposition of the Cu-Zn-Al hydrotalcite in synthetic air: **top**) TGA and DTGA profiles; **bottom**) EGA profiles for H_2O (m/z = 18) and CO_2 (m/z = 44) fragments. **B) Top**) TGA and **bottom**) DTGA patterns for the Cu-Zn-Al hydrotalcite decomposition in air at different heating rates used to derive data for the model fittings in Fig. 4. The inset in the top graph represents the amplification of the 225–350 °C region to show the trend; the shift into higher temperatures due to the heating rate's increase.

oxycarbonate, which could explain the weak CuO signals in the XRD. For the sake of clarity, CuO species were additionally characterised and can be seen in the H_2-TPR profile (Figure S2). No Al-based phases were detected by XRD and Al_2O_3 is thus present as an amorphous phase. Broad reflections in this material indicate that the sample is formed by low-crystalline and well-dispersed CuO and ZnO phases (and amorphous alumina); the metal cations were randomly distributed in the brucite layers before calcination, hence providing a good interdispersion of the final oxide phases. The amorphous alumina, with a composition of ca. 17 wt% (as Al_2O_3), can play a role to avoid sintering of the CuO and ZnO oxides, though its effect has been reported for the reduced catalysts[19]. Moreover, HT-CO_3 can avoid the sintering of the CuO and ZnO phases as well (discussed later in more detail). Both aspects would promote broad XRD reflections. Importantly, in support of the HT-CO_3, Behrens et al.[80] observed during the calcination of a Cu-Zn-Al hydrotalcite that the CuO crystallinity suddenly increased after removing the HT-CO_3, which indirectly proves the stabilization effect of the HT-CO_3 species.

The IR spectrum of the calcined material shows a splitting of the CO_3^{2-} ν_3 mode (Fig. 2B). Since at the calcination temperature nearly all (if not all) hydroxyls have been decomposed (Fig. 3A), the splitting of the ν_3 mode is due to the coordination of the CO_3^{2-} with the metal centres, thereby breaking its symmetry; i.e., it is interpreted as free carbonates in a Mg-Al hydrotalcite changing their coordination upon thermal treatment [83–85,87,89]. Elsewhere, the splitting has also been interpreted in other system as the insertion of oxygens from carbonates into the brucite layer of a thermally treated hydrotalcite, which conclusion was drawn by comparing the IR spectrum with that of dawsonite ($NaAl(OH)_2CO_3$), and the splitting

is the result of the lack of symmetry induced by the local environment [92]. The band at 877 cm^{-1} (946 cm^{-1} in the hydrotalcite) can be ascribed to Al-OH deformation [93]. The presence of the v_3 splitting and its splitting value (Δv_3 = 139 cm^{-1}) implies that the carbonates are strongly bonded (monodentate) to the metal cations [38,94].

There is a further band, v_1 mode (symmetrical stretching) at 1076 cm^{-1}. This vibrational mode is inactive when the CO_3^{2-} ion holds its full symmetry [95,96]. Therefore, its activation is evidence of a loss of symmetry of the carbonate groups. From literature observations, the v_1 mode in hydrotalcites becomes visible when the CO_3^{2-} loses symmetry following a rearrangement in the interlayer space, where the CO_3^{2-} coordinate metal centres in the interlayer space [83–85], or when the CO_3^{2-} groups have inserted oxygens into the brucite-like layer upon partial dehydroxylation [92]. In these cases, the structures were still layered which helps to understand that the CO_3^{2-} symmetry is not significantly lost, which explains why the v_1 band intensity is weak. However, Kannan et al. [91] reported the IR spectra of Cu-rich hydrotalcite upon calcination with an intense v_1 band development upon heating, which was ascribed to the reduced symmetry of carbonate groups. They suggested the formation of an oxycarbonate based on the TGA data (high decomposition temperature of the HT-CO_3) and v_3 IR bands, yet the strong v_1 activation was not discussed. However, we think that the v_1 activation is another proof for the oxycarbonate formation. A weak v_1 band has been reported for aurichalcite upon calcination (possessing strongly coordinating carbonates; also visible in the native aurichalcite), whereas this was absent in the calcined zincian malachite (with non-coordinating free carbonates) [38]. In our system, the v_1 band is very intense and indicates that the symmetry loss of the CO_3^{2-} groups is more severe and hence may be taking part in a more stable structure, than the corresponding from aurichalcite. Further evidence of the v_1 activation can be found in the structure of the hydroxycarbonate malachite [$Cu_2(CO_3)(OH)_2$] [40,97,98], which contains structural carbonates that connect wavy layers in the (101) planes. The IR spectrum of malachite was resolved by Schmidt and Lutz [99] employing $Cu_2(OD)_2CO_3$ to avoid the strong OH deformation bands; the v_1 was active and located at 1085 cm^{-1}, i.e., very close to the value we observed at 1076 cm^{-1}. As such, it is reasonable to suggest that the carbonates in the calcined Cu-Zn-Al material are integrated in the structure where they form an oxycarbonate, a topic that will be studied by DFT later within a model system.

3.3. Thermo-kinetics of the high-temperature carbonate decomposition

To understand better the nature of the HT-CO_3 in the calcined Cu-Zn-Al material, in view of the high decomposition temperature and strong interaction with the oxides as revealed by the v_3 splitting and active v_1 mode, further experimental characterization was undertaken. For this, we evaluated the activation energy of the CO_3^{2-} decomposition, and the resulting values were compared to conventional metal carbonates. The apparent activation energies (E_{Act}^{App}) were calculated for the well-resolved α, β and γ processes depicted in Fig. 3A, using two methods (Kissinger and Ozawa-Flynn-Wall) to crosscheck the results. To this end, a series of thermal analyses were carried out at various heating rates and the patterns are shown in Fig. 3B. The corresponding plots of the Kissinger and Ozawa-Flynn-Wall models are given in Fig. 4A and 4B, and the values are compiled in Tables S1 and S2. Table 1 provides a summary of the final results.

In general, there is good agreement between both methods that give comparable values, with step γ showing a more pronounced difference. The value for this process is very high regardless of the method (416 versus 532 kJ/mol), which is crucial for our interpretation, but it is not entirely clear which method provides a more accurate parameter. In the work of Tarasov et al. [100] a value of 464 kJ/mol can be deduced (reported as E/R = 55.8 × 10^3 K) for the activation energy of the high-temperature carbonates in a Cu-Zn aurichalcite, whilst a zincian malachite displayed a lower value of 297 kJ/mol. Elsewhere [38], a calcined zincian malachite and a calcined aurichalcite with the same composition (Cu/Zn = 80/20, at. and Cu/Zn = 40/60, at.) as in Tarasov et al. [100] displayed non-coordinating weak carbonates by IR. Therefore, the activation energy provides a quantitative value of the carbonate binding strength. The activation energy for our step γ is of the same order of magnitude as for aurichalcite decomposition, indicating strong bonding. Also relevant in our case is the comparison between steps β and γ. Step β (Fig. 3A) comprises the dehydroxylation but also the removal of the less-stable non-metal-coordinating carbonates [83–85]. This β process has an activation energy much lower than step γ (Table 1), with a value of around 200 kJ/mol, confirming the high stability and binding strength of the HT-CO_3 (step γ). Note that step δ (also HT-CO_3) would also have a high activation energy, but was not calculated due to the lack of resolution in the TGA patterns (Fig. 3B). When inspecting the literature, one can find typical values between 170 and 212 kJ/mol for the Cu hydroxy-carbonate [101], and between 159 and 280 kJ/mol for the Zn carbonate [102]. These values are in line with the carbonates in step β(194–203 kJ/mol), suggesting that the abnormally high activation energy for the γ process (416–532 kJ/mol) is neither characteristic of conventional carbonates nor of non-coordinating carbonates in hydrotalcites or hydroxycarbonates, as discussed earlier. Such a high energetic barrier can mean that the HT-CO_3 are very stable and likely form strong bonds with the oxide framework. Note that the apparent activation energy corresponds to the decomposition process, but it is not evident which step is rate determining, e.g., the local bonds or a physical process such as diffusion. In thermal solid-state reactions, diffusion of metal cations or anions can be the rate determining step [103], but no information is available in the literature on the rate determining step in our system. In our thermokinetic study, we preliminary ascribe the high apparent activation energy to the strength of the chemical bonds, based on a comparison made between two studies using two techniques for aurichalcite and zincian malachite [38,100], showing carbonates with different strengths.

In relation to the bonding preference of the HT-CO_3, there is some complexity on discerning whether they link CuO/ZnO or the Al(III) phase as well. The activation energy of the HT-CO_3 (step γ) has a large uncertainty, ranging from 416 to 532 kJ/mol depending on the method. While the reported value for a Cu-Zn aurichalcite, i.e., free of Al(III), lays between both (464 kJ/mol) [100]. Therefore, the role of Al(III) on the activation energy, and hence its bonding to the HT-CO_3, is not evident. Due to this limitation, we will later assume that the HT-CO_3 are associated to CuO and ZnO (DFT study). Moreover, the Al(III) phase is amorphous and cannot be modelled. The amount of HT-CO_3 can be deduced from Fig. 3A and it is 5.2 wt%. Considering the chemical analysis data, the following quantitative formula can be obtained, $M_6O_5(CO_3)$, where M is Cu plus Zn, which is comparable to the result from Tarasov et al. for a binary hydroxycarbonate [100] with a formula of $M_5O_4(CO_3)$. Considering that the HT-CO_3 links oxide particles at the interface, this HT-CO_3 concentration should be enough to suppress sintering.

In summary, the various techniques have shown HT-CO_3 being decomposed at high temperature (very stable), with well-dispersed CuO and ZnO phases, where the HT-CO_3 are strongly bonded to metal centres after calcination (v_3 splitting and its splitting value) and likely form part of the structure (v_3 splitting and v_1 activation). The high stability was verified by a thermo-kinetic

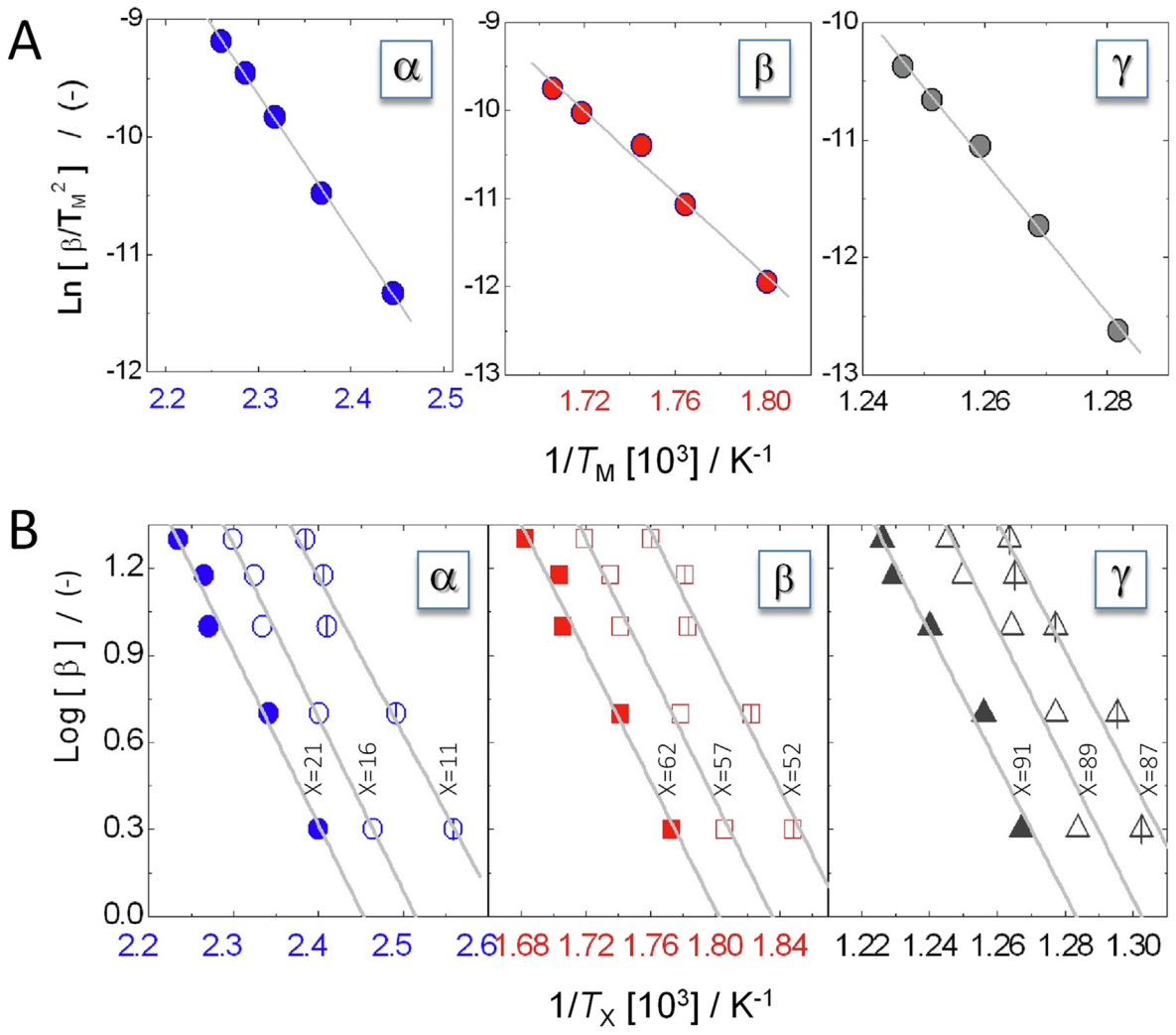

Fig. 4. Plots for the activation energy determination using the Kissinger (**A**) and Ozawa-Flynn-Wall (**B**) correlations of a Cu-Zn-Al hydrotalcite decomposition in air for the three processes (α, β and γ), according to the DTGA patterns in Fig. 3B. The Ozawa-Flynn-Wall correlation was applied at three different conversion levels (*X*). Raw data are given in Tables S1 and S2, with a summary in Table 1.

Table 1
Summary of the activation energies of the studied decomposition processes.

Process	Nature	*Ozawa-Flynn-Wall model*	*Kissinger model*
		$\overline{E_{Act}^{App}}$ (kJ/mol) [a]	E_{Act}^{App} (kJ/mol) [b]
α	Interlayer water removal	105 ± 5	97 ± 2
β	Dehydroxylation and partial CO_3^{2-} removal	203 ± 2	194 ± 14
γ	HT-CO_3 decomposition (first step)	416 ± 9	532 ± 19

a. Full set of data can be found in Table S2.
b. Full set of data can be found in Table S3.

study, showing very high apparent activation energies compared to conventional carbonates and non-coordinating carbonates, such as those in hydrotalcites/ hydroxycarbonates. The calcined material is an oxycarbonate where such HT-CO_3 may have a structural role in preventing sintering during calcination (and eventually during the reduction although this is not within the scope of this study). They can be bonded in two ways, either to a single oxide surface or linking the oxide particles, as e.g. M−CO−M'. In the latter case, the HT-CO_3 act as a glue by holding together the oxide domains, which could explain the lack of, or reduced, sintering during calcination and the broad XRD reflections (Fig. 1B). This hypothesis is schematically illustrated in Fig. 5. Based on this model, these linking carbonate groups would avoid or reduce the sintering of the oxide domains (Fig. 5B), forming a stable oxycarbonate. This model will be studied by DFT calculations using various parameters such as adsorption and adhesion energies, IR activity and CO_3 splitting (activation energy).

3.4. Background on the DFT studies

In order to obtain molecular level insight into the experimental findings, calculations based on the density functional theory (DFT) have been employed. Initially, the bulk and pristine surfaces of ZnO and CuO were modelled for the subsequent adsorption of carbonates and their incorporation at explicit interfaces. We have considered an explicit ZnO/CuO interface to assess the stability provided by additional carbonate groups. This interface is well-known in, for example, methanol synthesis catalysts and is suitable for this study as XRD results did not show the presence of any crystalline Al(III) phase (Fig. 1B).

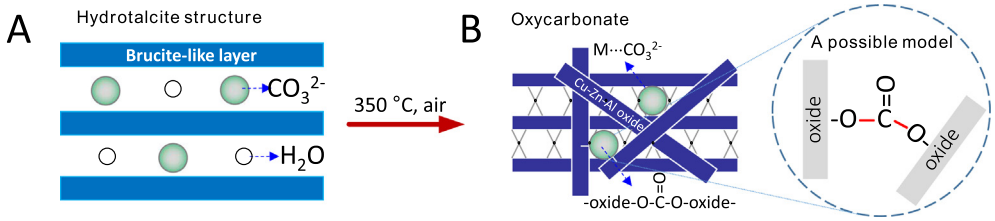

Fig. 5. Suggested model representing the thermal transformation of a Cu-Zn-Al hydrotalcite (**A**) into an oxycarbonate (**B**), including a possible configuration for the CO_3^{2-} insertion into the framework and linking the oxide particles. This model is later verified by DFT calculations.

Yet, the Al(III)-species can have an impact on several aspects of the calcination. Firstly, The HT-CO_3 may also be linked to the Al(III) phase but this is not possible to discern, in comparison with previous studies on Cu-Zn hydroxycarbonates, as explained in the previous section. It can also act as an amorphous spacer, avoiding the sintering of CuO and ZnO. These effects are out of the scope of the DFT study since amorphous Al_2O_3 cannot be modelled. For the sake of completeness, the Al_2O_3 effect can even be more complex in the reduced catalysts as pointed out elsewhere[8].

Below, the DFT study of the CuO, ZnO and interface will be discussed systematically.

3.5. Model structures

ZnO was modelled in the wurtzite phase (hexagonal structure, $P6_3mc$ space group, nr. 186), which is composed of tetrahedrally coordinated Zn^{2+} and O^{2-} ions stacked alternatingly along the c-axis. The experimental lattice parameters are **a** = **b** = 3.25 Å, and **c** = 5.21 Å [104], which are reproduced well at **a** = **b** = 3.24 Å and **c** = 5.21 Å, with the computational setup at B3LYP hybrid functional level. The Kohn-Sham electronic band gap is calculated at 3.31 eV as a direct transition at the Γ-point, which falls within the experimental range of 3.25 – 3.4 eV [105,106]. CuO adopts a monoclinic structure (space group C2/c, nr. 15) with Cu atoms organized in a square planar coordination arrangement with four surrounding O atoms, while each of the O atoms is located in the centre of a Cu distorted tetrahedron [107]. The calculated lattice parameters and angles are **a** = 4.67 Å, **b** = 3.42 Å, **c** = 5.14 Å, and β = 99.8° which correspond well to measured lattice parameters and angles of **a** = 4.72 Å, **b** = 3.40 Å, **c** = 5.04 Å, and β = 99.5° [108].

3.6. Surface adsorption

It is excruciatingly difficult to probe experimentally the exact composition and atomic arrangement of a heterostructure, and hence we need to assume a thermodynamically plausible interface from known examinations. As such, the ZnO (100) and the CuO (−111) surfaces were chosen to initially study the adsorption of selected carbonates and to create an explicit interface between the crystal planes to investigate the behaviour of the carbonate species therein. There is a clear rational for the choice of these surfaces. Together with the (110), (001), and (00−1) planes, the (100) surface of wurtzite constitutes one of the dominant low-index surfaces present in ZnO crystals [109]. Polarity plays an important role in the applications of ZnO surfaces, where the (001) and (00−1) slabs undergo complex reconstruction to cancel the inherent dipole present at the unreconstructed surfaces [110]. However, such reconstructed dipolar surfaces are usually less stable and we have therefore opted to use the non-polar symmetric ZnO (100) in this study (in the hexagonal notation labelled as the (10−10) surface). Similarly for cupric oxide, the two most dominant crystal planes present in its morphology are the (111) and (−111) surfaces [111], and the latter was chosen for our subsequent DFT analysis.

The mixed Zn- and O-terminated surface is the energetically most favourable (100) surface of ZnO, with a calculated surface energy of 1.15 J/m^2, which is in excellent agreement with SEM measurements that record a dominance of this surface in ZnO powder particles forming the sides of their hexagonal columns [112], as well as earlier theoretical works that calculated a surface energy of 1.16 J/m^2 [113]. The surface atoms undergo minimal rearrangement, with the top Zn atoms moving towards the surface in compensation for the reduced coordination environment caused by the missing tetrahedron corner oxygen atom when the surface was created. This slight relaxation results in a minimal alteration of the underlying electronic structure, with a calculated band gap of 3.15 eV, i.e., reduced by 0.15 eV compared to the corresponding bulk value. The surface energy of the relaxed CuO (−111) surface is computed at 0.94 J/m^2, with the geometry and electronic properties as documented in earlier work [114].

In order to establish a relevant baseline for subsequent comparison and to gain insight into the energetics of the processes, we initially adsorbed Na_2CO_3 and CO_3 individually on top of the selected ZnO (100) and CuO (−111) surfaces. The calculated adsorption energies of the two carbonate species as they bind to the oxide surfaces are reported in Table 2, together with their characteristic bond lengths. Sodium carbonate adsorbs onto the ZnO (100) surface in such a way that the Na atom binds the most prominent surface O atom, while two of the three O atoms surrounding C bind individual surface Zn atoms. The relaxed geometry is shown in Fig. 6A, together with the other structures. The bond distance d($Zn–O_{Na2CO3}$) = 2.00 Å is comparable to the length of the Zn–O bond in the bulk region of the ZnO (100) slab, which is 1.99 Å. The $Na–O_{ZnO}$ bond distance is measured at 2.18 Å, which is shorter than the bond length of $Na–O_{CO3}$ at 2.26 Å. These values together illustrate the strong binding of Na_2CO_3 to the ZnO (100) surface, which process releases as much as ca. 3 eV (ca. 269 kJ/mol).

The CO_3 species binds to ZnO (100) in a similar fashion as Na_2CO_3, with two O atoms binding to two surface Zn atoms with bond lengths of 1.96 Å and 2.01 Å (Table 2). The remaining O atom of the carbonate points away from the surface and does not participate actively in the adsorption process. Since the CO_3 species nominally exists in a −2 charge state, additional electron transfer takes place from the nearest neighbouring surface O atom to the carbonate ion for charge balance. This process leaves one hole behind on the surface O atom and one on the non-binding carbonate O, with each having a spin density (calculated from a Mulliken population analysis) of $\Delta O_{\uparrow-\downarrow} = 0.8\ e^-$. The resulting C–O carbonate bond is shortened by 0.03 – 0.06 Å and the calculated adsorption energy is reduced by ca. 0.5 eV compared to the adsorption energy of Na_2CO_3, releasing about 251 kJ/mol worth of energy upon CO_3 adsorption.

The adsorption of the selected carbonates onto the CuO (−111) surface is comparable geometrically as well as energetically to the attachment on the ZnO (100) surface. Na_2CO_3 binds strongly to the

Table 2
Calculated adsorption energies per molecule of carbonates bound to ZnO(100) and CuO(−111) surfaces as well as in between the ZnO(100)/CuO(−111) interface together with the length of the transition metal (TM) – carbonate oxygen bond and the carbon –carbonate oxygen specie bond. Values obtained using B3LYP.

System	E_b^{CP}(eV) / (kJ/mol)	d (TM - O_{CO3}) (Å)	d (C-O_{CO3}) (Å)
ZnO(100) + Na_2CO_3	−3.07 / −269.2	2.00/2.00	1.30/1.32/1.28
ZnO(100) + CO_3	−2.60 / −250.8	1.96/2.01	1.27/1.26/1.30
CuO(−111) + Na_2CO_3	−2.88 / −277.9	2.02/2.07	1.32/1.33/1.25
CuO(−111) + CO_3	−2.70 / −260.5	1.97/2.02	1.27/1.27/1.28
ZnO(100)/CuO(−111) + 1 · CO_3	−7.02 / −677.3	2.04/2.01/1.95	1.31/1.28/1.26
ZnO(100)/CuO(−111) + 2 · CO_3	−6.11 / −589.5	2.03/2.00/1.97	1.31/1.26/1.30

surface, with the two Na atoms forming a bond to two topmost O atoms and two of the three carbonate O atoms binding to the 3-fold coordinatively unsaturated surface Cu atoms. CO_3 binds in an analogous way as on the ZnO (100) surface, with two carbonate O atoms forming bonds with the most exposed under-coordinated Cu atoms. The heat of adsorption is similar in both cases (Table 2).

3.7. ZnO/CuO interface formation

An explicit ZnO/CuO interface was constructed by putting in contact the optimized ZnO (100) and CuO (−111) slabs. The lattice parameters were fixed to those of CuO, but the conclusions hold for the inverse situation just as well (where one would keep fixed the ZnO parameters). The final structure was more than 2.5 nm thick to reproduce the interface as well as the bulk-like regions in the employed model. The overall lattice mismatch is slightly under 6%, which is not negligible but within the experimental formation threshold. The ZnO/CuO hetero-interface structure after geometry relaxation is shown in Fig. 6B. The under-coordinated surface oxygen atoms constitute the main connecting point between the two oxide materials when in contact. After geometry relaxation, two of the four 3-fold coordinated surface

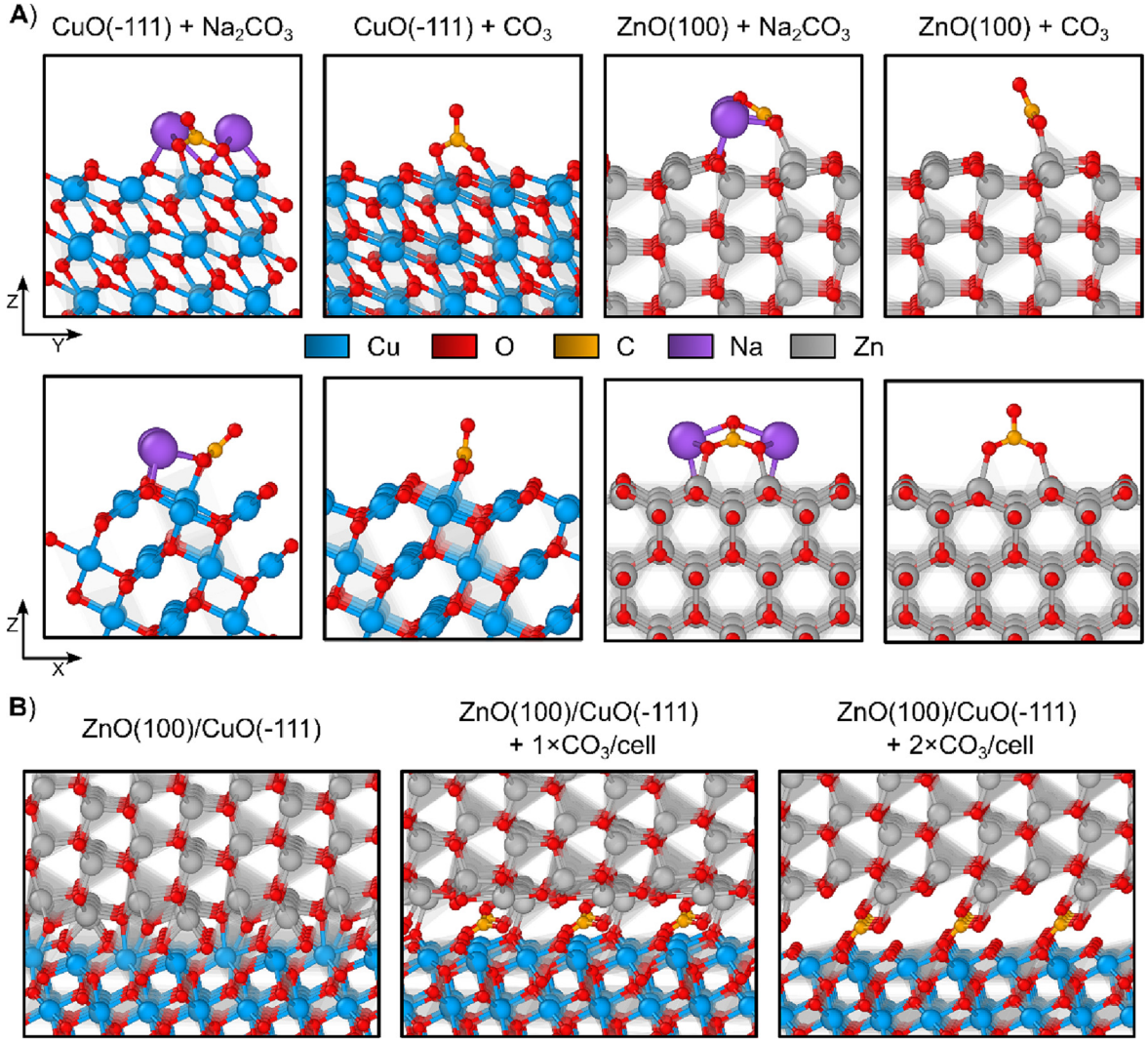

Fig. 6. Relaxed DFT geometries of: **A**) ZnO(100) and CuO(−111) surfaces with Na_2CO_3 and CO_3 molecules adsorbed on top, displaying the atomic positions and lattice geometry obtained using the B3LYP exchange–correlation functional; and **B**) epitaxially grown ZnO(100) atop of CuO(−111) without interlayer carbonates, and then with one and two interlayer carbonate molecules per unit cell, respectively.

Cu atoms formed a bond with two O atoms stemming from the ZnO side at distances of 1.98 Å. The remaining two ZnO surface oxygen atoms formed bonds with the 4-fold coordinated Cu atoms at distances of 2.15 Å, indicating a weaker interaction which is expected since the Cu atom in that configuration exists in a complete square planar coordination environment. Each Zn atom formed bridging bonds with two coordinatively unsaturated O atoms at distances of 1.95 Å and 2.10 Å, which are comparable to the *d* (Zn–O) = 1.97 Å bond length in bulk ZnO.

3.8. CO_3 interface binding

Upon CO_3 addition at the interface, i.e., within the ZnO (1 0 0) and CuO (−1 1 1) contact layer, growth of the two phases is greatly inhibited as is already noticeable upon visual inspection of the relaxed structures (middle and right of Fig. 6B). One carbonate molecule per unit cell is found to be sufficient to supress most bond formation between the two oxides, while two molecules per unit cell fully prevent the two oxides from contact and put them at a minimum distance of 3.3 Å apart. In both cases, the carbonate species binds one under-coordinated Cu atom with one O and two Zn atoms with the remaining two O atoms (Table 2). The calculated energies to incorporate the carbonate species in this structure are −7.02 eV and −6.11 eV for structures with one and two carbonates per unit cell, respectively. Those values identify the carbonate incorporation between the oxide layers as highly exothermic and, more importantly, highly probable. Furthermore, both energies are larger than the sum of individual adsorptions on the pristine surfaces (which crudely approximate −5.3 eV), elucidating the strong binding and incorporation of the carbonates at the interface. This finding is in agreement with the high stability of the interfacial carbonates discussed in the experimental results, which in addition link both oxide phases.

The calculated adhesion energy between the two oxide phases is 2.35 J/m^2, suggesting good structural compatibility between ZnO and CuO, and matching the experimentally noted likelihood of formation of this particular hetero-structure, as well as earlier ones [115,116]. The adhesion energy per interface of the ZnO/CuO hetero-structure with one and two carbonate species absorbed per unit cell is calculated at 1.13 J/m^2 and 1.81 J/m^2, respectively. Direct comparison between the pristine ZnO/CuO heterostructure and the carbonate-containing interface is, however, limited as the carbonated structure effectively contains two interfaces, one between CuO and CO_3 and another between CO_3 and ZnO. Summing those individual contributions, i.e., regarding the system as a whole, yields values of 2.26 J/m^2 and 3.62 J/m^2 for the structures with one and two carbonate species per unit cell, respectively. According to classical nucleation theory, the higher the adhesion energy, the higher the probability of heterogeneous nucleation compared to homogeneous nucleation [117]. In our case, the computed interfacial adhesion energy further suggests the likelihood of carbonate species being present between the oxide particles and thus preventing them from coalescing. In other words, the model proposed based on experimental measurements of carbonate ions stabilising particles and thus preventing sintering is indeed a favourable and plausible one. If the CuO/ZnO interfaces are stabilised in this way, the thermal sintering between CuO particles is avoided, or reduced.

3.9. Infrared activity

The vibrational features of the carbonate systems were assessed by calculating their infrared wavenumbers and intensities (Table S4). The spectrum of an isolated carbonate molecule contains four distinct vibrational groups (although carbonate ions are not stable as stand-alone entities, computationally they can be probed for comparison): low frequency in-plane bending (two modes, noted as ν_4), out of plane bending (one mode, ν_2), and asymmetric stretching (two modes, ν_3). The symmetric carbonate stretch (ν_1 at 1148 cm^{-1}) is infrared inactive when the carbonate molecule has its full symmetry, as outlined earlier (full spectrum shown in Fig. 7). This vibrational mode becomes active in all remaining systems under scrutiny where carbonates are attached. In freestanding sodium carbonate, ν_1 is shifted to much lower frequencies than those observed in the FTIR (Fig. 2B) and as such indicates no presence of this compound (or low concentration) in the final calcined material.

When CO_3 is adsorbed on top of the ZnO (1 0 0) and CuO (−1 1 1) surfaces, ν_1 is found at frequencies of 1093 cm^{-1} and 1078 cm^{-1}, respectively, although with a significantly reduced mode intensity (Fig. 7 inset). Such low spectral intensity of the ν_1 mode, together with the intensity difference between the two ν_3 carbonate peaks on the ZnO and CuO individual surfaces indicates that the measured IR spectra (Fig. 2B) cannot originate from these systems. However, in the model where carbonate is adsorbed at the ZnO/CuO interface, the ν_1 frequency is strongly activated and blue-shifted to 1109 cm^{-1} (compared to computed values of other systems in this study), which is in good agreement with the measured value of 1076 cm^{-1}, especially given the difference between the experimental conditions and assumptions of the theoretical model. Such a strong blue shift indicates strengthening of the intramolecular carbonate bonds due to intermolecular bonding features [118], further confirming the likelihood of CO_3 trapping between the oxide layers. Furthermore, the ν_3 is found split in the simulated spectrum with energies calculated at 1427 cm^{-1} and 1565 cm^{-1} ($\Delta\nu_3^{DFT}$ = 138 cm^{-1}), which again corresponds well with the measured values at 1412 cm^{-1} and 1551 cm^{-1} ($\Delta\nu_3^{experimental}$ = 139-cm^{-1}), respectively. The splitting value ($\Delta\nu_3$) typically corresponds to monodentate carbonate bonding [38,94], which was indeed found in the model structure (Fig. 6B middle and right). The observed activation of the ν_1 and splitting of the ν_3 carbonate vibrational mode confirm the possibility of CO_3 being inserted and stabilized into the oxide network. It should be noted that the intensities of the modelled ν_3 vibrations do not correspond exactly to those in the experimental spectrum (Fig. 2B) with a more pronounced intensity at 1551 cm^{-1}. This can be due to other effects in the real material that are not accounted for in the slab model, which, however, does not change the DFT evidence in favour of the HT-CO_3 as stabilizing species at the CuO/ZnO interface.

3.10. CO_3 dissociation

3.10.1. CO_3 dissociation on pristine ZnO (1 0 0) and CuO (−1 1 1) surfaces

To gain insight into the surface reactivity towards CO_3 dissociation into surface-bound CO_2 and O species, transition state calculations were performed to obtain reaction energies and activation barriers. The calculated minimum energy profile for CO_3 dissociation from the starting adsorbed configuration on the ZnO (1 0 0) and CuO (−1 1 1) surfaces is shown in Fig. 8A and 8B. Both reactions are found to be endothermic with energy barriers of 0.94 eV to dissociate CO_3 on the CuO (−1 1 1) surface and 1.40 eV to dissociate CO_3 on the ZnO (1 0 0) surface.

In the final configuration on the CuO (−1 1 1) surface, the O obtained from the dissociation forms two bonds with the under-coordinated surface cations at bond lengths of 1.92 Å and 2.00 Å, which is comparable to the Cu–O bulk bond length of 1.93 – 1.97 Å, indicating strong adsorption onto the surface. The remaining CO_2 binds via one O weakly to the surface, forming a Cu–O bond with a length of 2.32 Å. The overall reaction is found to be endothermic with a reaction energy of + 0.36 eV. On the ZnO

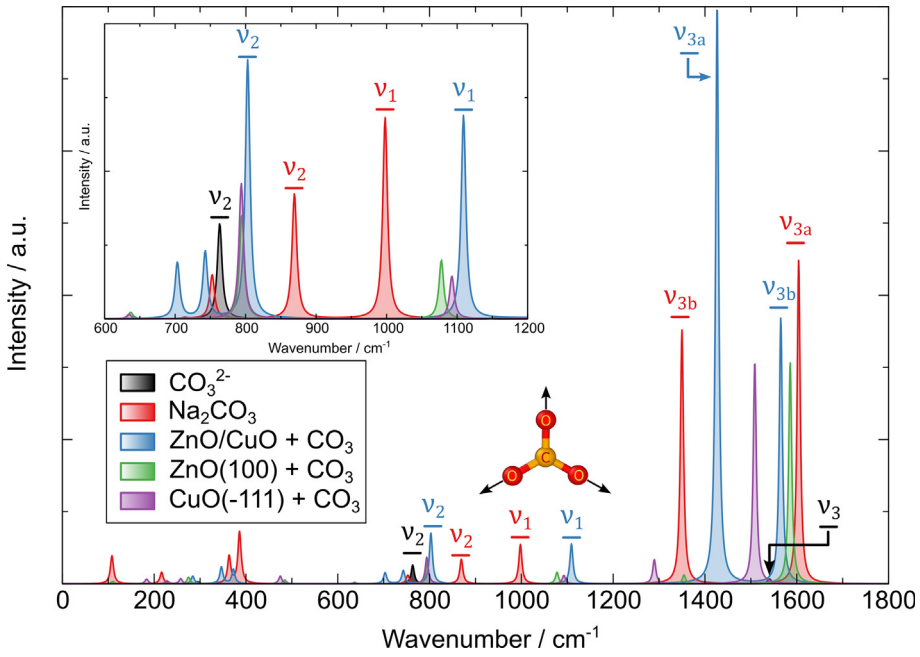

Fig. 7. Calculated infrared spectrum of CO_3^{2-} and Na_2CO_3 molecules as well as CO_3 fragment present at the ZnO and CuO surfaces as well as ZnO/CuO interface. The inset shows a zoom in the region of the ν_1 vibrational mode. The ν_1 mode (motif in figure) is infrared inactive when CO_3 possesses full symmetry and gets subsequently activated when that symmetry is reduced, either as part of the Na_2CO_3 molecule or the ZnO/CuO oxide network.

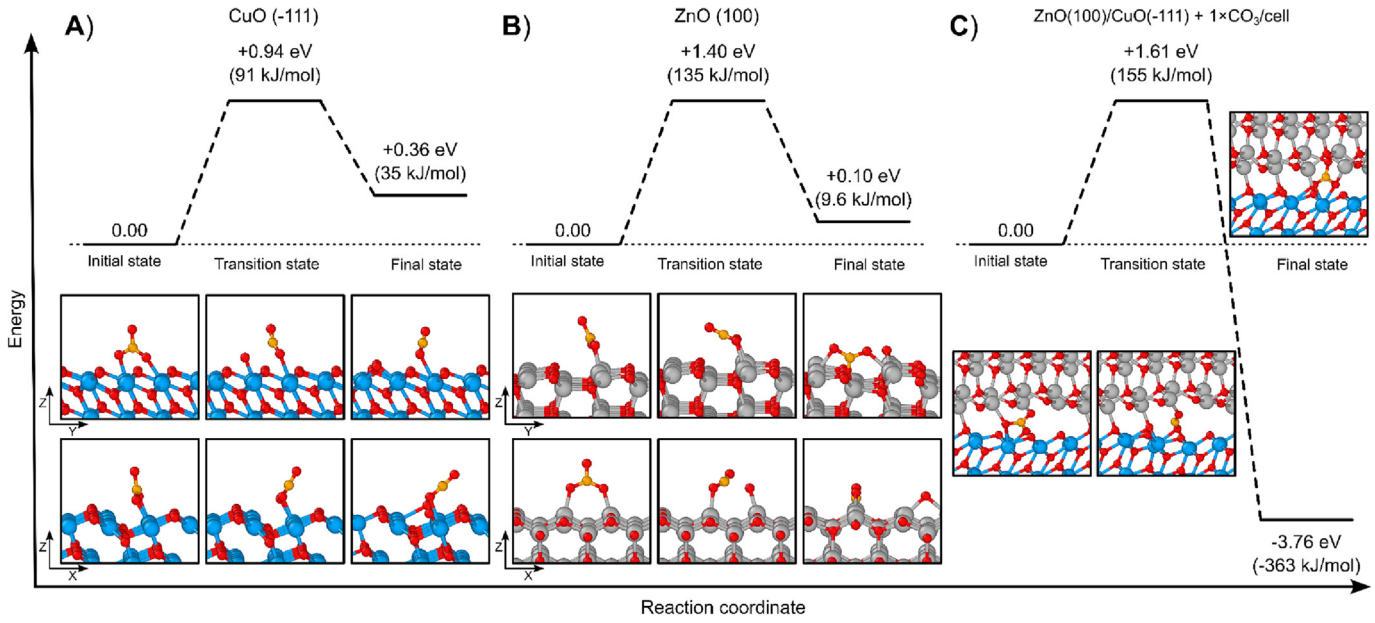

Fig. 8. Relative energy profile containing the activation barriers and reaction energies of carbonate dissociation into CO_2 and O at: A) the CuO(−1 1 1) surface, B) the ZnO(1 0 0) surface, and C) the ZnO/CuO interface. Values obtained using B3LYP and the distinguished reaction coordinate method.

(1 0 0) surface, the dissociated carbonate O binds two surface Zn atoms at distances of 2.05 Å and 1.96 Å, which is again comparable to the Zn-O bulk bond lengths. The newly formed CO_2 binds strongly to the surface where each of the two O atoms attaches to a surface cation and C binds one under-coordinated surface O. This process is endothermic with a cost of only + 0.10 eV, but a larger activation energy barrier compared to the carbonate dissociation process on the CuO surface.

Both reactions proceed via a two-step mechanism. The individual steps are interchangeable (i.e., their sequence is not important), which is why we will outline only one route. At first, one of the three carbonate oxygen atoms is detached to bind to a surface cation, followed by relaxation of the O–C–O carbonate angle into a suitable configuration to minimize the potential energy. On the CuO (−1 1 1) surface, that angle is found at 176.2° in a configuration where the molecule points away from the surface and binds weakly to the topmost cation, while on the ZnO (1 0 0) surface the analogous angle is 129.4°, i.e., closely resembling the internal CO_3 angle and binding firmly to the surface.

3.10.2. Transition state search at the ZnO/CuO interface

To further verify the proposed structural configuration and kinetics, transition state calculations were performed to elucidate the activation and dissociation mechanism of the carbonate ion

at the interface between ZnO and CuO. The calculated minimum energy profile for the proposed CO_3 dissociation mechanism from the starting carbonate structure incorporated at the ZnO/CuO interface is shown in Fig. 8C. The reaction initially follows the two-step pathway outlined earlier when dissociating carbonate on the pristine surfaces, with a consequent linearization of the O–C–O angle after one O is being detached from the carbonate group (crystal structure in the middle of Fig. 8C). The activation energy for this step is calculated at 1.61 eV (ca. 155 kJ/mol), which is larger than the same process on the pristine CuO of ZnO surfaces. Once the forces holding O and CO_2 together in the carbonate are weakened enough to prevent CO_3 from re-forming, the relaxation proceeds as a highly exothermic reaction releasing almost 3.8 eV (ca. 367 kJ/mol). Such a large reaction energy has not been noted in the literature and demonstrates the need for models with increasing complexity, such as our explicit interface system, which resembles as closely as possible the experiments, to take into account the chemical and physical interplay at the material interfaces. Importantly for this study, the activation energy for the carbonate splitting in the ZnO/CuO interface is higher than for the individual oxide counterparts, which is further evidence of the higher stability of the carbonates at the interface between the oxide particles, thus preventing them from growing.

As both the CuO and ZnO surfaces contain under-coordinated (reactive) transition metal sites, it is unfavourable for the CO_2 to exist as a self-contained molecule, counteracting the attractive Coulomb forces exerted onto it by the oxide network and between the ZnO and CuO layers themselves. In the final structure, one O from the newly formed CO_2 molecule binds two Cu atoms at d ($Cu–O_{CO3}$) = 2.01/2.21 Å with the other O atom binding one under-coordinated Zn atom at $d(Zn–O_{CO3})$ = 2.02 Å. The bond lengths of the newly formed (effective) carbonate (binding one O from the network) are $d(C–O_{CO3})$ = 1.25/1.32/1.28 Å, which is comparable to the intermolecular distances in the starting carbonate present at the ZnO/CuO interface (see Table 2). The third oxygen (from the carbonate before dissociation) binds to two under-coordinated Cu atoms at 1.89 Å and 1.92 Å, indicating strong adsorption at the CuO surface.

In addition, we note the role of the oxide framework flexibility when accommodating the dissociation of CO_3. In one scenario we simulated the splitting of CO_3 via the same two-step pathway outlined before but this time keeping the ZnO and CuO frameworks fixed until the CO_2 and O species have formed. Then we find that the oxygen detachment from the carbonate costs almost 3.5 eV and the linearization of the O–C–O bond angle adds an additional 1.4 eV. If we next allow the layers to relax to search for the final reaction configuration, we run into computational divergences and cannot obtain a stable structure. In other words, the barrier to dissociate CO_3 in an oxide network that is not allowed to breathe is considerably increased (around 4.9 eV or 473 kJ/mol) compared to the case where the ZnO/CuO network has full atomic flexibility and no stable structure for the final reaction products is found.

Not surprisingly, the complete dissociation reaction of CO_3 at the ZnO/CuO interface is extremely complex. However, we consider that the possible scenarios we have explored here are useful to understand the stability of the carbonate groups present within the oxide network.

3.11. Final remarks

Though the final reduced catalyst has not been studied here, it is worth to comment about it briefly. The final Cu dispersion or Cu-based active sites are the consequence of the full experimental history from the hydroxycarbonate/hydrotalcite structure, calcination and reduction conditions. It has been found that the HT-CO_3 are eliminated during the reduction step[33,38,41], but they can also influence the Cu dispersion or Cu-based active sites. Some hints about this can be found in the literature, showing a retarded CuO reduction in the presence of HT-CO_3 [41]. There is still some controversy between HT-CO_3 and copper surface area. While Schur et al. [28] shows that a HT-CO_3-free catalyst exhibited low copper surface area and low activity in methanol synthesis, Schumann et al.[38] did not obtain a lineal correlation between the HT-CO_3 and the copper surface area. This is perhaps related to the fact that these catalysts are structure-sensitive and copper surface area may not be a good descriptor of the catalytic activity. In other words, the correlation between the HT-CO_3 and the final catalyst activity is a more complex topic. Schumann et al. [38] found that catalysts with high HT-CO_3 concentration were less stable. Here, we observed that having two carbonate per unit cell in the ZnO/CuO interface rendered less stable carbonates than one per unit cell (Table 2), which is in agreement with Schumann et al. (bear in mind that they studied reduced catalysts). Hence, the type of carbonates (coordinating) and its concentration at the interface seem to play a role in the stability.

Overall, the literature has clearly evidenced the positive effect of the HT-CO_3 in the reaction. Here, we have proven their effect on the stability of the CuO and ZnO phases, which is a good precondition before the reduction step to have well-dispersed Cu-based phases. The possible role of the Al(III) in the calcination phase remains open.

4. Conclusions

The nature of the high-temperature carbonates in CuO/ZnO-based catalysts has been investigated experimentally using a model Cu-Zn-Al hydrotalcite, by means of XRD, thermal methods, IR spectroscopy and a thermo-kinetic study. Characterization revealed the presence of HT-CO_3 species, which are highly stable as shown by: 1) high decomposition temperature, 2) splitting of the ν_3 mode (IR), 3) activation of the ν_1 mode (IR) and 4) high apparent activation energy of their decomposition (shown by Kissinger and Ozawa-Flynn-Wall models). The calcined material displayed well-dispersed CuO and ZnO phases, with an amorphous Al-phase. It was hypothesized that such HT-CO_3 form stable oxycarbonates, where the carbonate groups act as a glue to link the oxide particles. This behaviour can explain the low or reduced thermal sintering during calcination and broad XRD reflections. This structural model is in line with other previous studies but investigations on the molecular features are absent in the literature. Therefore, we also studied the material from a molecular perspective using first-principles calculations based on the density functional theory. Alumina was not considered since it was amorphous (yet its additional effect on the calcination may still exist), whereas the ZnO/CuO interface is well-known in technical catalysts. Initially, model CuO and ZnO surfaces were defined and CO_3 surface adsorption was studied, before investigating the ZnO/CO_3/CuO interface, where the carbonates bind the CuO and ZnO surfaces. All DFT data provide evidence that such carbonate groups favourably bind the CuO and ZnO at the interface, rather than being present on the individual oxide surfaces. This was first shown by the adsorption and adhesion energies (larger), and the calculated IR spectrum matches the experimental spectrum (ν_3 and ν_1 vibrations); all this revealing strong carbonate interactions with the metal cations. Finally, the CO_3 dissociation reaction shows a higher activation energy when HT-CO_3 are at the interface, hence again showing its high stability. Our study provides new insights into the previously-reported concept of trapped high-temperature carbonates, which strongly suggests them to be part of the structure through a bonding mechanism between CuO and ZnO particles, thereby preventing thermal sintering during calcination.

Data availability

Data will be made available on request.

Declaration of Competing Interest

The authors declare that they have no known competing financial interests or personal relationships that could have appeared to influence the work reported in this paper.

Acknowledgments

IMC thanks the European Commission, grant number HPMF-CT-2002-01873 for financial support. IMC thanks Em. Prof. J. A. Moulijn for his support to carry out this project with state-of-the-art resources. A.Ž. and N.H.d.L. acknowledge the NWO ECHO grant (712.018.005) for funding and thank SURF (www.surf.nl) for access to the National Supercomputer Snellius.

Appendix A. Supplementary data

Supplementary data to this article can be found online at https://doi.org/10.1016/j.jcat.2023.06.032.

References

[1] B. Cornils, W.A. Herrmann, M. Muhler, in: C.-H. Wong (Ed.), Catalysis from A to Z: A Concise Encyclopedia, 3rd Edition, 3rd ed., Wiley-VCH Verlag GmbH, Weinheim, 2007.
[2] G. Anilkumar, S. Saranya (Eds.), Copper Catalysis in Organic Synthesis, Wiley-VCH Verlag GmbH, Weinheim, 2020.
[3] G.C. Chinchen, P.J. Denny, J.R. Jennings, M.S. Spencer, K.C. Waugh, Synthesis of Methanol, Appl. Catal. 36 (1988) 1–65, https://doi.org/10.1016/S0166-9834(00)80103-7.
[4] I. Melián-Cabrera, M. López Granados, P. Terreros, J.L. Fierro, CO_2 hydrogenation over Pd-modified methanol synthesis catalysts, Catal. Today. 45 (1998) 251–256, https://doi.org/10.1016/S0920-5861(98)00224-7.
[5] S. Fujita, S. Moribe, Y. Kanamori, M. Kakudate, N. Takezawa, Preparation of a coprecipitated Cu/ZnO catalyst for the methanol synthesis from CO_2 — effects of the calcination and reduction conditions on the catalytic performance, Appl. Catal. A Gen. 207 (2001) 121–128, https://doi.org/10.1016/S0926-860X(00)00616-5.
[6] I. Melián-Cabrera, M. López Granados, J.L.G. Fierro, Reverse Topotactic Transformation of a Cu–Zn–Al Catalyst during Wet Pd Impregnation: Relevance for the Performance in Methanol Synthesis from CO_2/H_2 Mixtures, J. Catal. 210 (2002) 273–284, https://doi.org/10.1006/jcat.2002.3676.
[7] M. Behrens, Meso- and nano-structuring of industrial Cu/ZnO/(Al_2O_3) catalysts, J. Catal. 267 (2009) 24–29, https://doi.org/10.1016/j.jcat.2009.07.009.
[8] M. Behrens, S. Zander, P. Kurr, N. Jacobsen, J. Senker, G. Koch, T. Ressler, R.W. Fischer, R. Schlögl, Performance Improvement of Nanocatalysts by Promoter-Induced Defects in the Support Material: Methanol Synthesis over Cu/ZnO:Al, J. Am. Chem. Soc. 135 (2013) 6061–6068, https://doi.org/10.1021/ja310456f.
[9] S.A. Kondrat, P.J. Smith, P.P. Wells, P.A. Chater, J.H. Carter, D.J. Morgan, E.M. Fiordaliso, J.B. Wagner, T.E. Davies, L. Lu, J.K. Bartley, S.H. Taylor, M.S. Spencer, C.J. Kiely, G.J. Kelly, C.W. Park, M.J. Rosseinsky, G.J. Hutchings, Stable amorphous georgeite as a precursor to a high-activity catalyst, Nature. 531 (2016) 83–87, https://doi.org/10.1038/nature16935.
[10] M. Behrens, F. Studt, I. Kasatkin, S. Kühl, M. Hävecker, F. Abild-Pedersen, S. Zander, F. Girgsdies, P. Kurr, B.-L. Kniep, M. Tovar, R.W. Fischer, J.K. Nørskov, R. Schlögl, The Active Site of Methanol Synthesis over Cu/ZnO/Al_2O_3 Industrial Catalysts, Science 336 (2012) 893–897, https://doi.org/10.1126/science.1219831.
[11] S.A. Kondrat, P.J. Smith, L. Lu, J.K. Bartley, S.H. Taylor, M.S. Spencer, G.J. Kelly, C.W. Park, C.J. Kiely, G.J. Hutchings, Preparation of a highly active ternary Cu-Zn-Al oxide methanol synthesis catalyst by supercritical CO_2 anti-solvent precipitation, Catal. Today. 317 (2018) 12–20, https://doi.org/10.1016/j.cattod.2018.03.046.
[12] N. Mota, R. Guil-Lopez, B.G. Pawelec, J.L.G. Fierro, R.M. Navarro, Highly active Cu/ZnO–Al catalyst for methanol synthesis: effect of aging on its structure and activity, RSC Adv. 8 (2018) 20619–20629, https://doi.org/10.1039/C8RA03291B.
[13] C. Rhodes, G.J. Hutchings, A.M. Ward, Water-gas shift reaction: finding the mechanistic boundary, Catal. Today. 23 (1995) 43–58, https://doi.org/10.1016/0920-5861(94)00135-O.
[14] J. Agrell, H. Birgersson, M. Boutonnet, I. Melián-Cabrera, R.M. Navarro, J.L.G. Fierro, Production of hydrogen from methanol over Cu/ZnO catalysts promoted by ZrO_2 and Al_2O_3, J. Catal. 219 (2003) 389–403, https://doi.org/10.1016/S0021-9517(03)00221-5.
[15] A. Küksal, E. Klemm, G. Emig, Reaction kinetics of the liquid-phase hydrogenation of succinic anhydride on CuZnO-catalysts with varying copper-to-zinc ratios in a three-phase slurry reactor, Appl. Catal. A Gen. 228 (2002) 237–251, https://doi.org/10.1016/S0926-860X(01)00978-4.
[16] L. He, H. Cheng, G. Liang, Y. Yu, F. Zhao, Effect of structure of CuO/ZnO/Al_2O_3 composites on catalytic performance for hydrogenation of fatty acid ester, Appl. Catal. A Gen. 452 (2013) 88–93, https://doi.org/10.1016/j.apcata.2012.11.039.
[17] S. Kattel, P.J. Ramírez, J.G. Chen, J.A. Rodriguez, P. Liu, Active sites for CO_2 hydrogenation to methanol on Cu/ZnO catalysts, Science 355 (2017) 1296–1299, https://doi.org/10.1126/science.aal3573.
[18] M. Zabilskiy, V.L. Sushkevich, D. Palagin, M.A. Newton, F. Krumeich, J.A. van Bokhoven, The unique interplay between copper and zinc during catalytic carbon dioxide hydrogenation to methanol, Nat. Commun. 11 (2020) 2409, https://doi.org/10.1038/s41467-020-16342-1.
[19] M.V. Twigg, Catalyst Handbook, 2nd Edition, Manson Publishing, London (1996), https://doi.org/10.1201/9781315138862.
[20] J.-D. Grunwaldt, A. Molenbroek, N.-Y. Topsøe, H. Topsøe, B. Clausen, In Situ Investigations of Structural Changes in Cu/ZnO Catalysts, J. Catal. 194 (2000) 452–460, https://doi.org/10.1006/jcat.2000.2930.
[21] J. Nakamura, Y. Choi, T. Fujitani, On the Issue of the Active Site and the Role of ZnO in Cu/ZnO Methanol Synthesis Catalysts, Top. Catal. 22 (2003) 277–285, https://doi.org/10.1023/A:1023588322846.
[22] M.V. Twigg, M.S. Spencer, Deactivation of Copper Metal Catalysts for Methanol Decomposition, Methanol Steam Reforming and Methanol Synthesis, Top. Catal. 22 (2003) 191–203, https://doi.org/10.1023/A:1023567718303.
[23] O. Martin, J. Pérez-Ramírez, New and revisited insights into the promotion of methanol synthesis catalysts by CO_2, Catal, Sci. Technol. 3 (2013) 3343–3352, https://doi.org/10.1039/C3CY00573A.
[24] N.D. Nielsen, A.D. Jensen, J.M. Christensen, The roles of CO and CO_2 in high pressure methanol synthesis over Cu-based catalysts, J. Catal. 393 (2021) 324–334, https://doi.org/10.1016/j.jcat.2020.11.035.
[25] T. Lunkenbein, F. Girgsdies, T. Kandemir, N. Thomas, M. Behrens, R. Schlögl, E. Frei, Bridging the Time Gap: A Copper/Zinc Oxide/Aluminum Oxide Catalyst for Methanol Synthesis Studied under Industrially Relevant Conditions and Time Scales, Angew. Chemie Int. Ed. 55 (2016) 12708–12712, https://doi.org/10.1002/anie.201603368.
[26] M.B. Fichtl, D. Schlereth, N. Jacobsen, I. Kasatkin, J. Schumann, M. Behrens, R. Schlögl, O. Hinrichsen, Kinetics of deactivation on Cu/ZnO/Al_2O_3 methanol synthesis catalysts, Appl. Catal. A Gen. 502 (2015) 262–270, https://doi.org/10.1016/j.apcata.2015.06.014.
[27] J. Wu, M. Saito, M. Takeuchi, T. Watanabe, The stability of Cu/ZnO-based catalysts in methanol synthesis from a CO_2-rich feed and from a CO-rich feed, Appl. Catal. A Gen. 218 (2001) 235–240, https://doi.org/10.1016/S0926-860X(01)00650-0.
[28] M. Schur, B. Bems, A. Dassenoy, I. Kassatkine, J. Urban, H. Wilmes, O. Hinrichsen, M. Muhler, R. Schlögl, Continuous Coprecipitation of Catalysts in a Micromixer: Nanostructured Cu/ZnO Composite for the Synthesis of Methanol, Angew. Chemie Int. Ed. 42 (2003) 3815–3817, https://doi.org/10.1002/anie.200250709.
[29] S.A. Kondrat, P.J. Smith, J.H. Carter, J.S. Hayward, G.J. Pudge, G. Shaw, M.S. Spencer, J.K. Bartley, S.H. Taylor, G.J. Hutchings, The effect of sodium species on methanol synthesis and water–gas shift Cu/ZnO catalysts: utilising high purity zincian georgeite, Faraday Discuss. 197 (2017) 287–307, https://doi.org/10.1039/C6FD00202A.
[30] G. Prieto, K.P. de Jong, P.E. de Jongh, Towards 'greener' catalyst manufacture: Reduction of wastewater from the preparation of Cu/ZnO/Al_2O_3 methanol synthesis catalysts, Catal. Today. 215 (2013) 142–151, https://doi.org/10.1016/j.cattod.2013.03.033.
[31] P.J. Smith, S.A. Kondrat, P.A. Chater, B.R. Yeo, G.M. Shaw, L. Lu, J.K. Bartley, S.H. Taylor, M.S. Spencer, C.J. Kiely, G.J. Kelly, C.W. Park, G.J. Hutchings, A new class of Cu/ZnO catalysts derived from zincian georgeite precursors prepared by co-precipitation, Chem. Sci. 8 (2017) 2436–2447, https://doi.org/10.1039/C6SC04130B.
[32] G. Prieto, J. Zečević, H. Friedrich, K.P. de Jong, P.E. de Jongh, Towards stable catalysts by controlling collective properties of supported metal nanoparticles, Nat. Mater. 12 (2013) 34–39, https://doi.org/10.1038/nmat3471.
[33] E. Frei, A. Gaur, H. Lichtenberg, C. Heine, M. Friedrich, M. Greiner, T. Lunkenbein, J. Grunwaldt, R. Schlögl, Activating a Cu/ZnO : Al Catalyst – Much More than Reduction: Decomposition, Self-Doping and Polymorphism, ChemCatChem. 11 (2019) 1587–1592, https://doi.org/10.1002/cctc.201900069.
[34] L. Pandit, A. Boubnov, G. Behrendt, B. Mockenhaupt, C. Chowdhury, J. Jelic, A. Hansen, E. Saraçi, E. Ras, M. Behrens, F. Studt, J. Grunwaldt, Unravelling the Zn-Cu Interaction during Activation of a Zn-promoted Cu/MgO Model Methanol Catalyst, ChemCatChem. 13 (2021) 4120–4132, https://doi.org/10.1002/cctc.202100692.
[35] T.M. Yurieva, Catalyst for methanol synthesis: Preparation and activation, React. Kinet. Catal. Lett. 55 (1995) 513–521, https://doi.org/10.1007/BF02073088.
[36] G.J. Millar, I.H. Holm, P.J.R. Uwins, J. Drennan, Characterization of precursors to methanol synthesis catalysts Cu/ZnO system, J. Chem. Soc. Faraday Trans. 94 (1998) 593–600, https://doi.org/10.1039/a703954i.

[37] S. Kühl, A. Tarasov, S. Zander, I. Kasatkin, M. Behrens, Cu-Based Catalyst Resulting from a Cu, Zn, Al Hydrotalcite-Like Compound: A Microstructural, Thermoanalytical, and In Situ XAS Study, Chem. - A Eur. J. 20 (2014) 3782–3792, https://doi.org/10.1002/chem.201302599.

[38] J. Schumann, A. Tarasov, N. Thomas, R. Schlögl, M. Behrens, Cu, Zn-based catalysts for methanol synthesis: On the effect of calcination conditions and the part of residual carbonates, Appl. Catal. A Gen. 516 (2016) 117–126, https://doi.org/10.1016/j.apcata.2016.01.037.

[39] B. Bems, M. Schur, A. Dassenoy, H. Junkes, D. Herein, R. Schlögl, Relations between Synthesis and Microstructural Properties of Copper/Zinc Hydroxycarbonates, Chem. - A Eur. J. 9 (2003) 2039–2052, https://doi.org/10.1002/chem.200204122.

[40] M. Behrens, F. Girgsdies, A. Trunschke, R. Schlögl, Minerals as Model Compounds for Cu/ZnO Catalyst Precursors: Structural and Thermal Properties and IR Spectra of Mineral and Synthetic (Zincian) Malachite, Rosasite and Aurichalcite and a Catalyst Precursor Mixture, Eur. J. Inorg. Chem. 2009 (2009) 1347–1357, https://doi.org/10.1002/ejic.200801216.

[41] J. Schumann, T. Lunkenbein, A. Tarasov, N. Thomas, R. Schlögl, M. Behrens, Synthesis and Characterisation of a Highly Active Cu/ZnO: Al Catalyst, ChemCatChem. 6 (2014) 2889–2897, https://doi.org/10.1002/cctc.201402278.

[42] T. Hatakeyama, L. Zhenhai, Handbook of Thermal Analysis, John Wiley & Sons Ltd, Chichester, UK, 1998.

[43] I. Melián-Cabrera, Temperature control in DRIFT cells used for in situ and operando studies: where do we stand today?, Phys Chem. Chem. Phys. 22 (2020) 26088–26092, https://doi.org/10.1039/D0CP04352D.

[44] V. Solsona, S. Morales-de la Rosa, O. De Luca, H. Jansma, B. van der Linden, P. Rudolf, J.M. Campos-Martín, M.E. Borges, I. Melián-Cabrera, Solvent Additive-Induced Deactivation of the Cu–ZnO(Al_2O_3)-Catalyzed γ-Butyrolactone Hydrogenolysis: A Rare Deactivation Process, Ind. Eng. Chem. Res. 60 (2021) 15999–16010, https://doi.org/10.1021/acs.iecr.1c04080.

[45] R. Dovesi, V.R. Saunders, C. Roetti, R. Orlando, C.M. Zicovich-Wilson, F. Pascale, B. Civalleri, K. Doll, N.M. Harrison, I.J. Bush, P. D'Arco, M. Llunell, M. Causà, Y. Noël, L. Maschio, A. Erba, M. Rerat, S. Casassa, CRYSTAL17 User's Manual, (2017).

[46] R. Dovesi, A. Erba, R. Orlando, C.M. Zicovich-Wilson, B. Civalleri, L. Maschio, M. Rérat, S. Casassa, J. Baima, S. Salustro, B. Kirtman, Quantum-mechanical condensed matter simulations with CRYSTAL, Wiley Interdiscip. Rev. Comput. Mol. Sci. 8 (2018) 1–36, https://doi.org/10.1002/wcms.1360.

[47] F. Pascale, C.M. Zicovich-Wilson, F. López Gejo, B. Civalleri, R. Orlando, R. Dovesi, The calculation of the vibrational frequencies of crystalline compounds and its implementation in the CRYSTAL code, J. Comput. Chem. 25 (2004) 888–897, https://doi.org/10.1002/jcc.20019.

[48] C.M. Zicovich-Wilson, F. Pascale, C. Roetti, V.R. Saunders, R. Orlando, R. Dovesi, Calculation of the vibration frequencies of α-quartz: The effect of Hamiltonian and basis set, J. Comput. Chem. 25 (2004) 1873–1881, https://doi.org/10.1002/jcc.20120.

[49] A.D. Becke, A new mixing of Hartree-Fock and local density-functional theories, J. Chem. Phys. 98 (1993) 1372–1377, https://doi.org/10.1063/1.464304.

[50] C. Lee, W. Yang, R.G. Parr, Development of the Colle-Salvetti correlation-energy formula into a functional of the electron density, Phys. Rev. B. 37 (1988) 785–789, https://doi.org/10.1103/PhysRevB.37.785.

[51] J.E. Jaffe, N.M. Harrison, A.C. Hess, Ab initio study of ZnO (1010) surface relaxation, Phys. Rev. B. 49 (1994) 11153–11158, https://doi.org/10.1103/PhysRevB.49.11153.

[52] J.E. Jaffe, A.C. Hess, Hartree-Fock study of phase changes in ZnO at high pressure, Phys. Rev. B. 48 (1993) 7903–7909, https://doi.org/10.1103/PhysRevB.48.7903.

[53] K. Doll, N. Harrison, Chlorine adsorption on the Cu(111) surface, Chem. Phys. Lett. 317 (2000) 282–289, https://doi.org/10.1016/S0009-2614(99)01362-7.

[54] L. Valenzano, F.J. Torres, K. Doll, F. Pascale, C.M. Zicovich-Wilson, R. Dovesi, Ab initio study of the vibrational spectrum and related properties of crystalline compounds; the case of $CaCO_3$ calcite, Zeitschrift Fur Phys, Chemie. 220 (2006) 893–912, https://doi.org/10.1524/zpch.2006.220.7.893.

[55] R. Dovesi, C. Roetti, C. Freyria-Fava, M. Prencipe, V.R. Saunders, On the elastic properties of lithium, sodium and potassium oxide. An ab initio study, Chem. Phys. 156 (1991) 11–19, https://doi.org/10.1016/0301-0104(91)87032-Q.

[56] R. Dovesi, M. Causa', R. Orlando, C. Roetti, V.R. Saunders, Ab initio approach to molecular crystals: A periodic Hartree–Fock study of crystalline urea, J. Chem. Phys. 92 (1990) 7402–7411. doi:10.1063/1.458592.

[57] H.J. Monkhorst, J.D. Pack, Special points for Brillouin-zone integrations, Phys. Rev. B. 13 (1976) 5188–5192, https://doi.org/10.1103/PhysRevB.13.5188.

[58] S. Grimme, J. Antony, S. Ehrlich, H. Krieg, A consistent and accurate ab initio parametrization of density functional dispersion correction (DFT-D) for the 94 elements H-Pu, J. Chem. Phys. 132 (2010), https://doi.org/10.1063/1.3382344.

[59] S. Grimme, S. Ehrlich, L. Goerigk, Effect of the damping function in dispersion corrected density functional theory, J. Comput. Chem. 32 (2011) 1456–1465, https://doi.org/10.1002/jcc.21759.

[60] S. Grimme, A. Hansen, J.G. Brandenburg, C. Bannwarth, Dispersion-Corrected Mean-Field Electronic Structure Methods, Chem. Rev. 116 (2016) 5105–5154, https://doi.org/10.1021/acs.chemrev.5b00533.

[61] A. Togo, I. Tanaka, $\texttt{Spglib}$: a software library for crystal symmetry search, (2018). http://arxiv.org/abs/1808.01590.

[62] Y. Hinuma, G. Pizzi, Y. Kumagai, F. Oba, I. Tanaka, Band structure diagram paths based on crystallography, Comput. Mater. Sci. 128 (2017) 140–184, https://doi.org/10.1016/j.commatsci.2016.10.015.

[63] A. Stukowski, Visualization and analysis of atomistic simulation data with OVITO–the Open Visualization Tool, Model. Simul. Mater. Sci. Eng. 18 (2010), https://doi.org/10.1088/0965-0393/18/1/015012.

[64] S.F. Boys, F. Bernardi, The calculation of small molecular interactions by the differences of separate total energies. Some procedures with reduced errors, Mol. Phys. 19 (1970) 553–566, https://doi.org/10.1080/00268977000101561.

[65] J. Scaranto, G. Mallia, N.M. Harrison, An efficient method for computing the binding energy of an adsorbed molecule within a periodic approach. the application to vinyl fluoride at rutile TiO_2(1 1 0) surface, Comput. Mater. Sci. 50 (2011) 2080–2086, https://doi.org/10.1016/j.commatsci.2011.02.011.

[66] S.P. Ong, W.D. Richards, A. Jain, G. Hautier, M. Kocher, S. Cholia, D. Gunter, V.L. Chevrier, K.A. Persson, G. Ceder, Python Materials Genomics (pymatgen): A robust, open-source python library for materials analysis, Comput. Mater. Sci. 68 (2013) 314–319, https://doi.org/10.1016/j.commatsci.2012.10.028.

[67] W. Sun, G. Ceder, Efficient creation and convergence of surface slabs, Surf. Sci. 617 (2013) 53–59, https://doi.org/10.1016/j.susc.2013.05.016.

[68] R. Tran, Z. Xu, B. Radhakrishnan, D. Winston, W. Sun, K.A. Persson, S.P. Ong, Surface energies of elemental crystals, Sci. Data. 3 (2016), https://doi.org/10.1038/sdata.2016.80.

[69] A. Zur, T.C. McGill, Lattice match: An application to heteroepitaxy, J. Appl. Phys. 55 (1984) 378–386, https://doi.org/10.1063/1.333084.

[70] P. Pulay, G. Fogarasi, Geometry optimization in redundant internal coordinates, J. Chem. Phys. 96 (1992) 2856–2860, https://doi.org/10.1063/1.462844.

[71] J. Simons, J. Nichols, Strategies for walking on potential energy surfaces using local quadratic approximations, Int. J. Quantum Chem. 38 (1990) 263–276, https://doi.org/10.1002/qua.560382427.

[72] A. Rimola, C.M. Zicovich-Wilson, R. Dovesi, P. Ugliengo, Search and Characterization of Transition State Structures in Crystalline Systems Using Valence Coordinates, J. Chem. Theory Comput. 6 (2010) 1341–1350, https://doi.org/10.1021/ct900680f.

[73] C.M. Zicovich-Wilson, M.L. San Román, A. Ramírez-Solís, Mechanism of F − Elimination from Zeolitic D4R Units: A Periodic B3LYP Study on the Octadecasil Zeolite, J. Phys. Chem. C. 114 (2010) 2989–2995, https://doi.org/10.1021/jp9088244.

[74] S. Miyata, The Syntheses of Hydrotalcite-Like Compounds and Their Structures and Physico-Chemical Properties I: The Systems Mg^{2+}-Al^{3+}-NO_3^-, Mg^{2+}-Al^{3+}-Cl^-, Mg^{2+}-Al^{3+}-Cl^-, Clays Clay Miner. 23 (1975) 369–375, https://doi.org/10.1346/CCMN.1975.0230508.

[75] F. Cavani, F. Trifirò, A. Vaccari, Hydrotalcite-type anionic clays: Preparation, properties and applications, Catal. Today. 11 (1991) 173–301, https://doi.org/10.1016/0920-5861(91)80068-K.

[76] D.P. Debecker, E.M. Gaigneaux, G. Busca, Exploring, Tuning, and Exploiting the Basicity of Hydrotalcites for Applications in Heterogeneous Catalysis, Chem. - A Eur. J. 15 (2009) 3920–3935, https://doi.org/10.1002/chem.200900060.

[77] S. Nishimura, A. Takagaki, K. Ebitani, Characterization, synthesis and catalysis of hydrotalcite-related materials for highly efficient materials transformations, Green Chem. 15 (2013) 2026, https://doi.org/10.1039/c3gc40405f.

[78] J.G. Nunan, P.B. Himelfarb, R.G. Herman, K. Klier, C.E. Bogdan, G.W. Simmons, Methanol synthesis catalysts based on cesium/copper/zinc oxide/metal oxide (metal = aluminum, chromium, gallium): genesis from coprecipitated hydrotalcite-like precursors, solid-state chemistry, morphology, and stability, Inorg. Chem. 28 (1989) 3868–3874, https://doi.org/10.1021/ic00319a023.

[79] I. Melián-Cabrera, M.L. Granados, J.L.G. Fierro, Pd-Modified Cu–Zn Catalysts for Methanol Synthesis from CO_2/H_2 Mixtures: Catalytic Structures and Performance, J. Catal. 210 (2002) 285–294, https://doi.org/10.1006/jcat.2002.3677.

[80] M. Behrens, I. Kasatkin, S. Kühl, G. Weinberg, Phase-Pure Cu, Zn, Al Hydrotalcite-like Materials as Precursors for Copper rich Cu/ZnO/Al_2O_3 Catalysts, Chem. Mater. 22 (2010) 386–397, https://doi.org/10.1021/cm9029165.

[81] P. Gao, F. Li, N. Zhao, F. Xiao, W. Wei, L. Zhong, Y. Sun, Influence of modifier (Mn, La, Ce, Zr and Y) on the performance of Cu/Zn/Al catalysts via hydrotalcite-like precursors for CO_2 hydrogenation to methanol, Appl. Catal. A Gen. 468 (2013) 442–452, https://doi.org/10.1016/j.apcata.2013.09.026.

[82] I. Melián-Cabrera, M. López Granados, J.L.G. Fierro, Structural Reversibility of a Ternary CuO-ZnO-Al_2O_3ex Hydrotalcite-Containing Material During Wet Pd Impregnation, Catal. Lett. 84 (2002) 153–161, https://doi.org/10.1023/A:1021467617700.

[83] I. Melián-Cabrera, M. López Granados, J.L.G. Fierro, Thermal decomposition of a hydrotalcite-containing Cu–Zn–Al precursor: thermal methods combined with an in situ DRIFT study, Phys. Chem. Chem. Phys. 4 (2002) 3122–3127, https://doi.org/10.1039/b201996e.

[84] J. Pérez-Ramírez, G. Mul, F. Kapteijn, J.A. Moulijn, In situ investigation of the thermal decomposition of Co–Al hydrotalcite in different atmospheres, J. Mater. Chem. 11 (2001) 821–830, https://doi.org/10.1039/b009320n.

[85] J. Pérez-Ramírez, G. Mul, J. Moulijn, In situ Fourier transform infrared and laser Raman spectroscopic study of the thermal decomposition of Co–Al and Ni–Al hydrotalcites, Vib. Spectrosc. 27 (2001) 75–88. doi:10.1016/S0924-2031(01)00119-9.

[86] S. Miyata, Physico-Chemical Properties of Synthetic Hydrotalcites in Relation to Composition, Clays Clay Miner. 28 (1980) 50–56, https://doi.org/10.1346/CCMN.1980.0280107.
[87] L. Pesic, S. Salipurovic, V. Markovic, D. Vucelic, W. Kagunya, W. Jones, Thermal characteristics of a synthetic hydrotalcite-like material, J. Mater. Chem. 2 (1992) 1069, https://doi.org/10.1039/jm9920201069.
[88] W. Yang, Y. Kim, P.K.T. Liu, M. Sahimi, T.T. Tsotsis, A study by in situ techniques of the thermal evolution of the structure of a Mg–Al–CO_3 layered double hydroxide, Chem. Eng. Sci. 57 (2002) 2945–2953, https://doi.org/10.1016/S0009-2509(02)00185-9.
[89] J. Pérez-Ramírez, S. Abelló, N.M. van der Pers, Memory Effect of Activated Mg–Al Hydrotalcite. In Situ XRD Studies during Decomposition and Gas-Phase Reconstruction, Chem. - A Eur. J. 13 (2007) 870–878, https://doi.org/10.1002/chem.200600767.
[90] J. Zhang, Y.F. Xu, G. Qian, Z.P. Xu, C. Chen, Q. Liu, Reinvestigation of Dehydration and Dehydroxylation of Hydrotalcite-like Compounds through Combined TG-DTA-MS Analyses, J. Phys. Chem. C. 114 (2010) 10768–10774, https://doi.org/10.1021/jp103115q.
[91] S. Kannan, V. Rives, H. Knözinger, High-temperature transformations of Cu-rich hydrotalcites, J. Solid State Chem. 177 (2004) 319–331, https://doi.org/10.1016/j.jssc.2003.08.023.
[92] T. Stanimirova, I. Vergilov, G. Kirov, N. Petrova, Thermal decomposition products of hydrotalcite-like compounds: low-temperature metaphases, J. Mater. Sci. 34 (1999) 4153–4161, https://doi.org/10.1023/A:1004673913033.
[93] J. Theo Kloprogge, R.L. Frost, Infrared emission spectroscopic study of the thermal transformation of Mg-, Ni- and Co-hydrotalcite catalysts, Appl. Catal. A Gen. 184 (1999) 61–71, https://doi.org/10.1016/S0926-860X(99)00084-8.
[94] K.I. Hadjiivanov, G.N. Vayssilov, Characterization of oxide surfaces and zeolites by carbon monoxide as an IR probe molecule, in, Adv. Catal. (2002) 307–511, https://doi.org/10.1016/S0360-0564(02)47008-3.
[95] M.J. Hernandez-Moreno, M.A. Ulibarri, J.L. Rendon, C.J. Serna, IR characteristics of hydrotalcite-like compounds, Phys. Chem. Miner. 12 (1985) 34–38, https://doi.org/10.1007/BF00348744.
[96] J.C. Lavalley, Infrared spectrometric studies of the surface basicity of metal oxides and zeolites using adsorbed probe molecules, Catal. Today. 27 (1996) 377–401, https://doi.org/10.1016/0920-5861(95)00161-1.
[97] P. Süsse, Verfeinerung der Kristallstruktur des Malachits, $Cu_2(OH)_2CO_3$, Acta Crystallogr. 22 (1967) 146–151, https://doi.org/10.1107/S0365110X67000222.
[98] D. Stoilova, V. Koleva, V. Vassileva, Infrared study of some synthetic phases of malachite ($Cu_2(OH)_2CO_3$)–hydrozincite ($Zn_5(OH)_6(CO_3)_2$) series, Spectrochim, Acta Part A Mol. Biomol. Spectrosc. 58 (2002) 2051–2059, https://doi.org/10.1016/S1386-1425(01)00677-1.
[99] M. Schmidt, H.D. Lutz, Hydrogen bonding in basic copper salts: a spectroscopic study of malachite, $Cu_2(OH)_2CO_3$, and brochantite, $Cu_4(OH)_6SO_4$, Phys. Chem. Miner. 20 (1993), https://doi.org/10.1007/BF00202247.
[100] A. Tarasov, J. Schumann, F. Girgsdies, N. Thomas, M. Behrens, Thermokinetic investigation of binary Cu/Zn hydroxycarbonates as precursors for Cu/ZnO catalysts, Thermochim. Acta. 591 (2014) 1–9, https://doi.org/10.1016/j.tca.2014.04.025.
[101] M. Reading, D. Dollimore, The application of constant rate thermal analysis to the study of the thermal decomposition of copper hydroxy carbonate, Thermochim. Acta. 240 (1994) 117–127, https://doi.org/10.1016/0040-6031(94)87034-9.
[102] B. V L'vov, Mechanism and kinetics of thermal decomposition of carbonates, Thermochim. Acta. 386 (2002) 1–16, https://doi.org/10.1016/S0040-6031(01)00757-2.
[103] M.N. Rahaman, Ceramic Processing and Sintering, 2nd ed., CRC Press, Boca Raton, 2003. doi:10.1201/9781315274126.
[104] K. Kihara, G. Donnay, Anharmonic thermal vibrations in ZnO, Can. Mineral. 23 (1985) 647–654.
[105] K. Harun, N.A. Salleh, B. Deghfel, M.K. Yaakob, A.A. Mohamad, DFT + U calculations for electronic, structural, and optical properties of ZnO wurtzite structure: A review, Results Phys. 16 (2020), https://doi.org/10.1016/j.rinp.2019.102829.
[106] H. Sim, J. Lee, S. Cho, E.S. Cho, S.J. Kwon, A study on the band structure of ZnO/CdS heterojunction for CIGS solar-cell application, J. Semicond. Technol. Sci. 15 (2015) 267–275, https://doi.org/10.5573/JSTS.2015.15.2.267.
[107] F. Marabelli, G.B. Parravicini, Evidence of localized states in the optical gap of CuO, Phys. B Condens. Matter. 199–20 (1994) 255–256, https://doi.org/10.1016/0921-4526(94)91802-3.
[108] A.A. Samokhvalov, N.A. Viglin, B.A. Gizhevskij, N.N. Loshkareva, V. V. Osipov, N.I. Solin, Y.P. Sukhorukov, Low-mobility charge carriers in CuO, Zhurnal Eksp. i Teor. Fiz. (ISSN 0044-4510). 103 (1993) 951–961. http://adsabs.harvard.edu/abs/1993ZhETF.103..951S.
[109] H. Moormann, D. Kohl, G. Heiland, Variations of work function and surface conductivity on clean cleaved zinc oxide surfaces by annealing and by hydrogen adsorption, Surf. Sci. 100 (1980) 302–314, https://doi.org/10.1016/0039-6028(80)90374-X.
[110] D. Mora-Fonz, T. Lazauskas, M.R. Farrow, C.R.A. Catlow, S.M. Woodley, A.A. Sokol, Why Are Polar Surfaces of ZnO Stable?, Chem Mater. 29 (2017) 5306–5320, https://doi.org/10.1021/acs.chemmater.7b01487.
[111] A.K. Mishra, A. Roldan, N.H. De Leeuw, CuO Surfaces and CO_2 Activation: A Dispersion-Corrected DFT+U Study, J. Phys. Chem. C. 120 (2016) 2198–2214, https://doi.org/10.1021/acs.jpcc.5b10431.
[112] C. Wöll, The chemistry and physics of zinc oxide surfaces, Prog. Surf. Sci. 82 (2007) 55–120, https://doi.org/10.1016/j.progsurf.2006.12.002.
[113] A. Wander, F. Schedin, P. Steadman, A. Norris, R. McGrath, T.S. Turner, G. Thornton, N.M. Harrison, Stability of polar oxide surfaces, Phys. Rev. Lett. 86 (2001) 3811–3814, https://doi.org/10.1103/PhysRevLett.86.3811.
[114] A. Živković, G. Mallia, H.E. King, N.H. de Leeuw, N.M. Harrison, Mind the Interface Gap: Exposing Hidden Interface Defects at the Epitaxial Heterostructure between CuO and Cu_2O, ACS Appl. Mater. Interfaces. 14 (2022) 56331–56343, https://doi.org/10.1021/acsami.2c16889.
[115] P. Nayak, S. Kumar, I. Sinha, K.K. Singh, ZnO/CuO nanocomposites from recycled printed circuit board: preparation and photocatalytic properties, Environ. Sci. Pollut. Res. 26 (2019) 16279–16288, https://doi.org/10.1007/s11356-019-04986-6.
[116] M. Haddad, A. Belhadi, L. Boudjellal, M. Trari, Photocatalytic hydrogen production on the hetero-junction CuO/ZnO, Int. J. Hydrogen Energy. 46 (2021) 37556–37563, https://doi.org/10.1016/j.ijhydene.2020.11.053.
[117] M. Bruno, L. Pastero, A. Cotellucci, D. Aquilano, Epitaxy: a methodological approach to the study of an old phenomenon, CrystEngComm. 24 (2022) 4165–4173, https://doi.org/10.1039/D2CE00340F.
[118] H.D. Lutz, H. Haeuseler, Infrared and Raman spectroscopy in inorganic solids research, J. Mol. Struct. 511–512 (1999) 69–75, https://doi.org/10.1016/S0022-2860(98)00630-9.